Earth, Planets and Space

FULL PAPER Open Access

Strong-motion characteristics of two 2022 M 6.5 + disastrous earthquakes in the southern longitudinal valley, Taiwan

Yen-Yu Lin[1,2,3], Yi-Ying Wen[4,5*], Chun-Te Chen[6] and Yin-Tung Yen[6]

Abstract

Two disastrous earthquakes, the M_L 6.6 Guanshan and M_L 6.8 Chihshang earthquakes, called the 0917 and 0918 events, respectively, occurred in the southern longitudinal valley (LV) of eastern Taiwan within a 17-h interval in 2022. In the present study, we document the observed strong ground motions and damage distributions and analyze the source properties of both events via broadband (0.2 ~ 10 Hz), near-field, strong-motion seismic records. The results of Empirical Green's function (EGF) analysis reveal that the 0917 event ruptured to the south in a single strong-motion generation area (SMGA), with a size of 47.04 km^2, and that the 0918 event ruptured to the north through two SMGAs, with a combined size of 80.16 km^2. The SMGA models explain the observed velocity pulses that caused severe damage well. Using the source-scanning algorithm technique, we obtain the centroid locations of both events on the west-dipping Central Range Fault (CNF), indicating that the 0917 and 0918 events had southward directivity and northward directivity, respectively, which are consistent with the results from the EGF method. We summarize that the velocity pulses of both events could be attributed to rupture directivity, high stress drops, and shallow ruptures from the obtained SMGA(s). Combined with the findings of previous studies of moderate-to-large earthquakes occurring in the LV, seismic hazard assessment and mitigation are important because of the interaction between the west-dipping CNF and the east-dipping LV fault, especially for the shallow part above a depth of 10 km.

Keywords Rupture directivity, Strong motion generation area, Stress drop

*Correspondence:
Yi-Ying Wen
yiyingwen@gmail.com
Full list of author information is available at the end of the article

Graphical Abstract

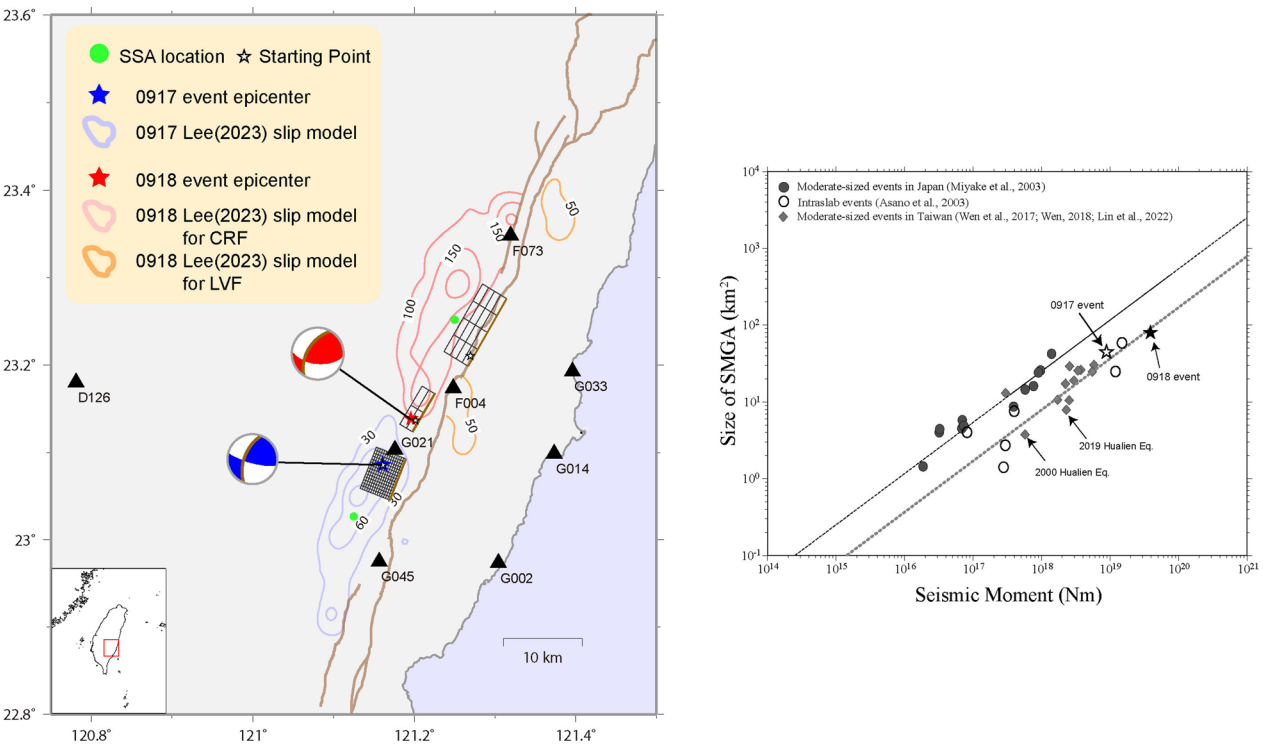

1 Background

Two disastrous events, the M_L 6.6 Guanshan (called the 0917 event hereafter) and the M_L 6.8 Chihshang earthquakes (called the 0918 event hereafter) on September 17 and 18, 2022, respectively (Fig. 1), struck the southern longitudinal valley (LV) of eastern Taiwan. The hypocenters were located at 121.161°E, 23.084°N, with a focal depth of 8.61 km, for the 0917 event, and at 121.196°E, 23.137°N, with a focal depth of 7.81 km, for the 0918 event, as reported by the Central Weather Administration (CWA). The moment tensor solutions of the Broadband Array in Taiwan for Seismology (BATS) (Jian et al. 2018) revealed that the mechanisms of these two events were strike slips with minor thrust motions on a fault plane with a high dip angle (Fig. 2; Table 1). These two shallow events caused intense ground shaking and resulted in unexpected disasters and severe damage along the LV (marked as diamonds in Figs. 2 and 3).

The LV is defined as a suture zone between the Philippine Sea plate and the Eurasian plate and extends 150 km between Hualien and Taitung Counties in eastern Taiwan (Yu and Kuo 2001; Hickman et al. 2002). According to geodesic studies, the LV accommodates horizontal shortening at a rate of approximately 30–40 mm/year (Yu et al. 1997; Yu and Kuo 2001), which is also accompanied by high seismicity. The

(See figure on next page.)

Fig. 1 Distributions of the stations as well as the Central Weather Administration (CWA) epicenters (stars) and locations (solid circles) according to the source-scanning algorithm (SSA) for the 0917 and 0918 events. The blue symbols represent the 0917 event, and the red symbols represent the 0918 event. The 2000 (black star) and 2019 (white star) Hualien earthquakes are also shown. The red triangles and green squares represent the locations of the TSMIP and P-alert networks, respectively. The red lines indicate the identified active fault traces from the Central Geological Survey (CGS) 2021 version. The cross and circular symbols indicate the seismicity after the 0917 (2022/9/17 13:41:20 ~ 2022/9/18 06:44:14 UTC) and 0918 (2022/9/18 06:44:14 ~ 2022/9/25 00:00:00 UTC) events, respectively. The selected waveforms in the figure are the observed velocities with PGVs > 60 cm/s for both events. The maximum PGVs and the time scale are presented

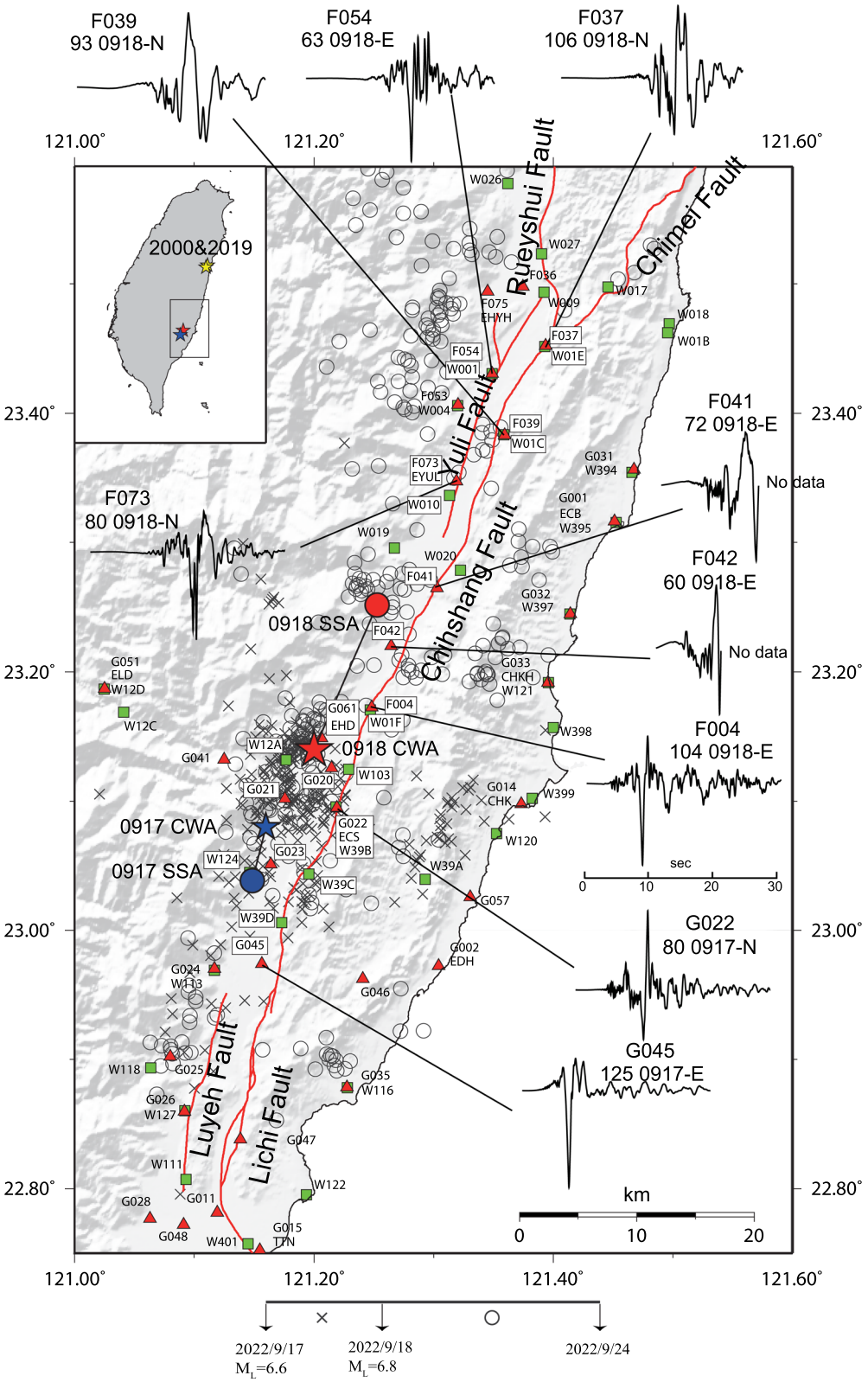

Fig. 1 (See legend on previous page.)

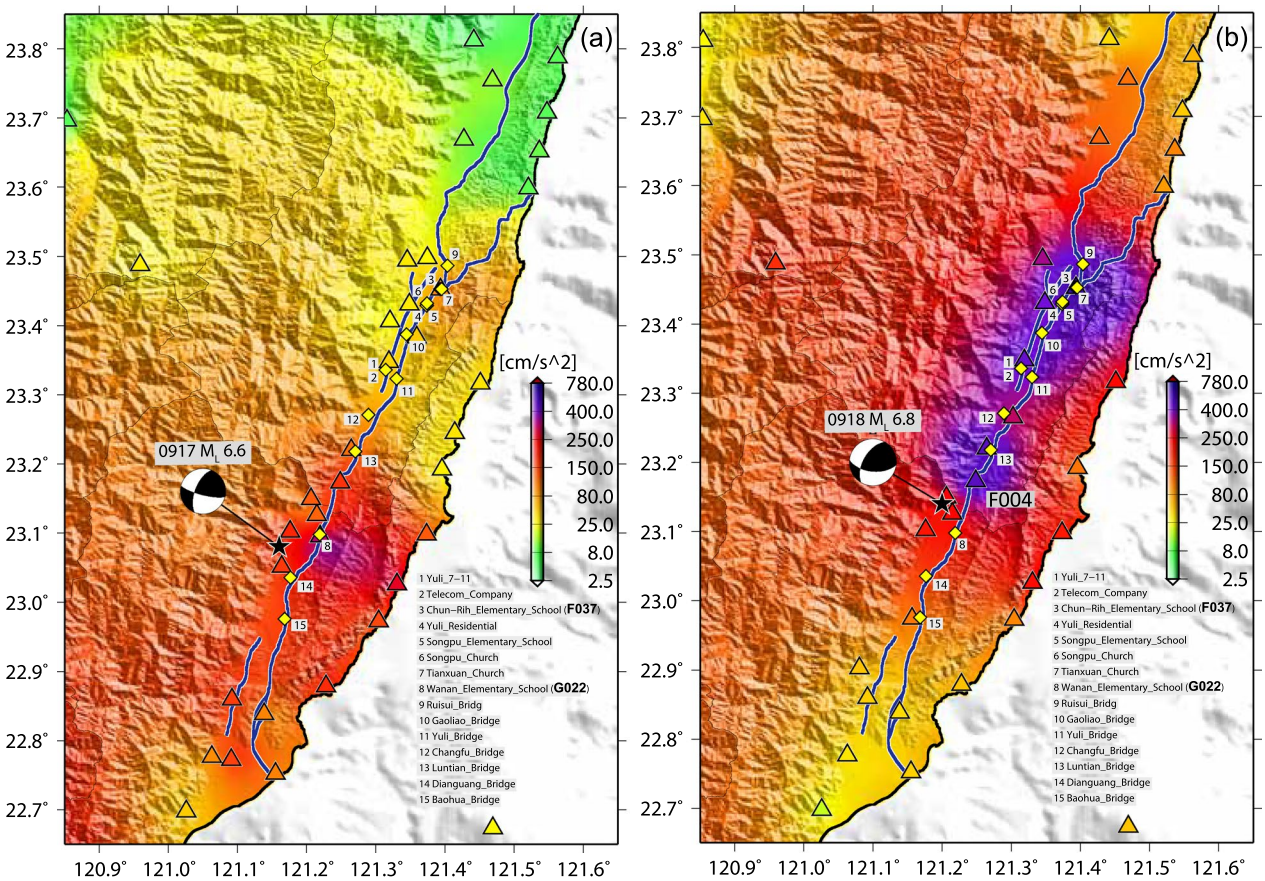

Fig. 2 PGA distributions of the (**a**) 0917 and (**b**) 0918 events, where the black star represents the epicenter, triangles represent strong-motion stations, and yellow diamonds represent damaged buildings (without distinguishing whether damage occurred via the 0917 or 0918 event). The blue line is the active fault line of the CGS 2021 version. The color contours of the PGA are derived through interpolation based on data acquired from strong-motion stations within the specified range. The interpolation is conducted via GMT version 4.5.16, with a grid spacing of 1 km

Table 1 Earthquake parameters for the 2022 Guanshan earthquake (0917 event) and 2022 Chihshang earthquake (0918 event) and related REF/EGF events

Date	17 Sep 2022 (0917 event)	13 Sep 2022 (0917 REF)	21 Sep 2022 (0917 EGF)	18 Sep 2022 (0918 event)	18 Sep 2022 (0918 REF)	18 Sep 2022 (0918 EGF)
Epicenter	121.161°E 23.084°N	121.154°E 23.078°N	121.151°E 23.068°N	121.196°E 23.137°N	121.194°E 23.146°N	121.195°E 23.141°N
Depth	8.61 km	9.23 km	14.12 km	7.81 km	7.45 km	7.81 km
Fault plane (strike, dip, rake)	201/62/15		206/90/30	210/56/40		201/75/39
M_L	6.6	4.7	4.8	6.8	4.8	5.7
M_0	8.76×10^{18} Nm[a]		3.20×10^{15} Nm[b]	3.87×10^{19} Nm[a]		9.30×10^{16} Nm[b]

The epicenters and fault plane solutions were determined by the CWA and BATS solutions, respectively. The seismic moments were determined as follows: [a]Global CMT and [b]BATS solutions

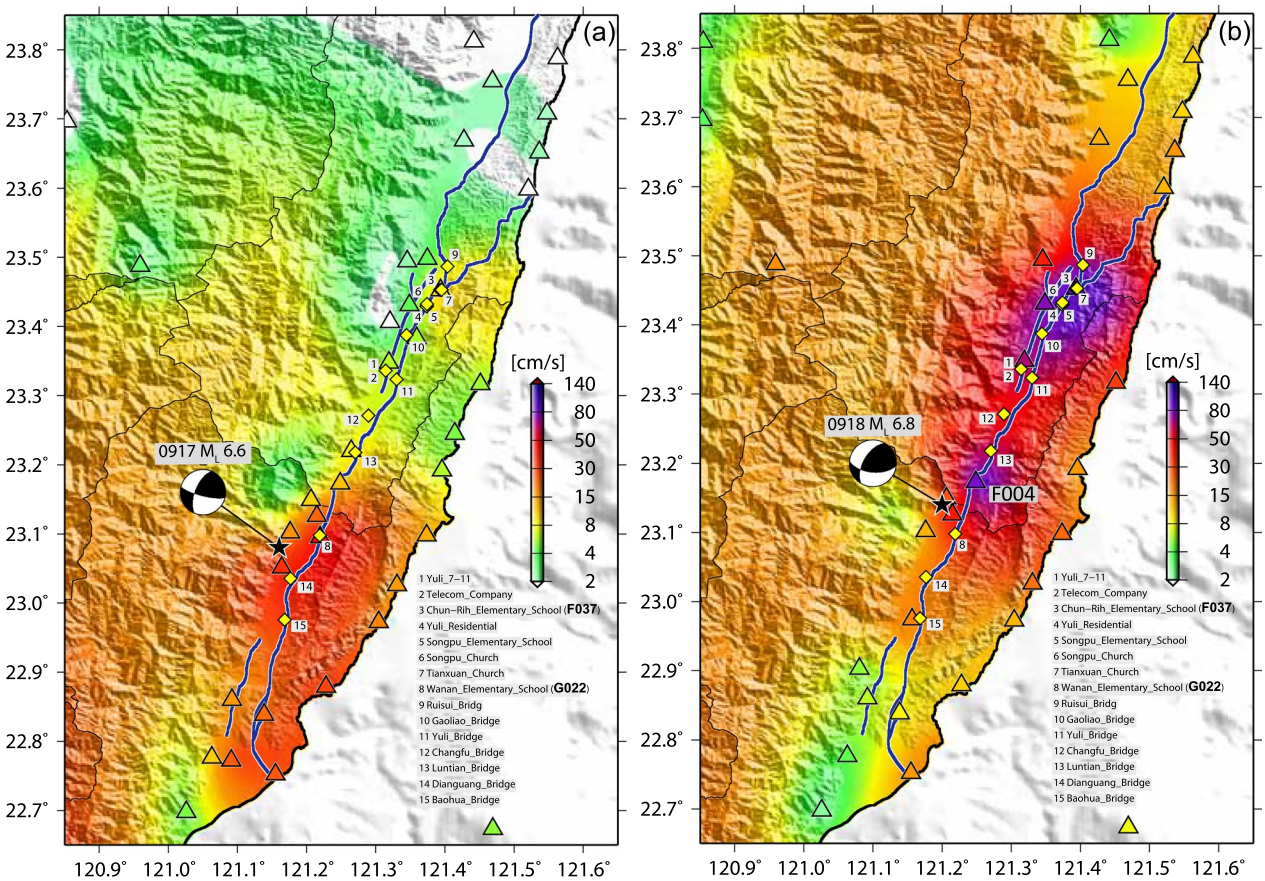

Fig. 3 PGV distributions of the (**a**) 0917 and (**b**) 0918 events, where the black star represents the epicenter, triangles represent strong-motion stations, and yellow diamonds represent damaged buildings (without distinguishing whether damage occurred via the 0917 or 0918 event). The blue line is the active fault line of the CGS 2021 version. The color contours of the PGV are derived through interpolation based on data acquired from strong-motion stations within the specified range. The interpolation is conducted via GMT version 4.5.16, with a grid spacing of 1 km

east-dipping faults [southern part of the LV fault, named LVF hereafter, defined by Shyu et al. (2020), and the Chihshang fault, defined by the Central Geological Survey, CGS (2022)] are considered the main seismogenic faults due to plate collision along the LV suture boundary. Despite the low activity and absence of surface outcrops, previous studies have suggested the existence of the west-dipping Central Range Fault (CNF) bounding the western margin of the LV (Biq 1965; Lee et al. 2003; Shyu et al. 2006). Several moderate-sized events that occurred in the northern CNF, e.g., the 2013 M_L 6.4 Ruisui, 2018 Mw 6.4 Hualien, and 2019 M_L 6.3 Hualien earthquakes, have been reported (Wen et al. 2016; Lin et al. 2022 and all other studies for these events), as well as the 2006 Mw 6.1 Taitung earthquake in the southern CNF (Wu et al. 2006; Mozziconacci et al. 2013). Similar to the 2006 Taitung event, the focal mechanisms and aftershock distributions suggested that both the 0917 and 0918 events ruptured mainly on the west-dipping CNF within 17 h (Fig. 1; Lee et al. 2023).

Two previous studies reported slip distributions on the fault(s) for both events. Yagi et al. (2023) adopted teleseismic waveforms and determined the source process of both events via the potency density tensor inversion method. Lee et al. (2023) obtained a finite-fault slip model by jointly using teleseismic and several local strong-motion waveforms. Both studies focused only on records with a low-frequency (or long-period) bandwidth, which is less than 0.5 Hz. The slip patterns from both studies are similar. The 0917 and 0918 events ruptured from the epicenter to the south and north, respectively. Unlike previous studies, we are interested in

documenting seismic records from local strong-motion networks and damage situations for both events, as well as in obtaining the source properties of both events, with a focus on waveforms with a frequency bandwidth of 0.2 ~ 10 Hz. This is because waveforms with high-frequency bandwidth signals (> 0.5 Hz) (e.g., velocity pulses with a period of 1 ~ 2 s) and large amplitudes (> 60 cm/s) may cause severe damage to buildings and structures, which are important and interesting for most earthquake engineering applications (Construction and Planning Agency 2011; Wu et al. 2016). Mechanisms producing such waveforms containing high-frequency signals with large amplitudes are key for seismic hazards and need to be further investigated using high-frequency seismic records.

To determine source properties using local, dense strong-motion networks, we first employ empirical Green's function (EGF) analysis. The well-known EGF method is one of the conventional techniques used to investigate the source properties of earthquakes by eliminating the effects of site amplification and propagation paths (e.g., Velasco et al. 1994; Lay and Wallace 1995; Ammon et al. 2005). Irikura (1986) developed an EGF method, which assumes a characterized source model consisting of one or more rectangular slip patches, to simulate broadband strong-motion records (up to 10 Hz). Miyake et al. (2001, 2003) defined the characteristic slip patch with relatively large slip velocities within the total rupture area as the "strong-motion generation area (SMGA)". Taking advantage of dense strong-motion station networks in Taiwan, several moderate-to-large events have been well studied via the EGF method, including the 2013 Ruisui earthquake (Wen et al. 2016), eight Nantou events that occurred in 1999 and 2013 (Wen et al. 2017), the 2010 Jiashian and 2016 Meinong earthquakes (Wen et al. 2020), and the 2000 and 2019 Hualien earthquakes (Lin et al. 2022). Second, we apply the source-scanning algorithm (SSA) to evaluate the centroid location and directivity pattern via the maximum amplitude in the displacement records. The SSA method has been considered in many seismic source studies at event locations (Kao and Shan 2004; 2007; Kao et al. 2008; Liao et al. 2012). It has also worked well in distinguishing the centroid of multiple subevents within a large event (Kan et al. 2010; Lin et al. 2018, 2022). Both independent methods for analyzing strong-motion records in different frequency ranges help us better understand the source properties of the 0917 and 0918 earthquakes.

1.1 Data

We use strong-motion records of the Taiwan Strong-Motion Instrumentation Program (TSMIP) network managed by the CWA and deployed on a free field (Liu et al. 1999; Liu and Tsai 2005). In addition, we consider data from the P-alert strong-motion network operated by National Taiwan University. P-alert instruments, which are designed for early warning systems, are deployed inside school buildings (Wu et al. 2013). The sensors of both networks are broadband accelerometers, in which the frequency band from 0.1 to 10 Hz is flat in the instrument response. Figure 1 shows the distributions of the TSMIP and P-alert networks (marked by triangles and squares, respectively) in the source area. In addition to the free-field TSMIP strong-motion data, we also consider the non-free-field network of P-alerts, because the available stations around the study area are insufficient due to the following two conditions: (i) because the Central and Coast Ranges to the west and east of the LV restrict deployments, the stations are deployed only along the LV and the coastline east of the Coast Range and (ii) the 0918 event caused extremely high amplitudes of ground motion, resulting in some records for both networks being interrupted owing to power shortages and/or internet disconnection (e.g., stations F041 and F042; Fig. 1).

1.2 Distributions of strong ground motions and damage

Figures 2 and 3 present the distributions of the geometric mean values of the peak ground acceleration (PGA) and peak ground velocity (PGV) for 0917 and 0918 events, respectively. The geometric mean is defined as the square root of the product of the maximum values of the horizontal components (NS and EW). The highest ground motion values for the 0917 event were recorded at the Wanan Elementary School station (G022, which is the diamond marker labeled No. 8), with PGAs of 273 cm/s^2 and 397 cm/s^2 for the E–W and N–S components, respectively (Fig. 2a). The observed PGVs are 28 cm/s and 80 cm/s for the E–W and N–S components, respectively (Fig. 3a). The highest ground motion values for the 0918 event were recorded at the Chun-Rih Elementary School station (F037, which is the diamond marker labeled No. 3), with even higher PGAs of 622 cm/s^2 and 651 cm/s^2 for the E–W and N–S components, respectively (Fig. 2b), and PGVs of 76 cm/s and 111 cm/s for the E–W and N–S components, respectively (Fig. 3b). Although the waveforms at stations F041 and F042 were not completely recorded due to communication interruption during the 0918 event (Fig. 1), the geometric mean PGA and PGV were extracted on the basis of incomplete waveform data. The geometric mean PGA at F041 is at least 320 cm/s^2,

and at F042, it is at least 490 cm/s^2, with PGVs both larger than 60 cm/s. Furthermore, Fig. 1 shows the observed waveforms with extremely high PGVs (PGV > 60 cm/s) for the N–S or E–W components. These observed velocity waveforms seem to carry an obvious velocity pulse with a large amplitude.

Overall, the ground motion values south of the epicenter of the 0917 event are relatively high, and the values north of the epicenter of the 0918 event are also relatively high (Fig. 2). The shakemaps for the earthquake sequences show asymmetric distributions with respect to the distance from the epicenter. Although the distance between the epicenters of events 0917 and 0918 is only ~ 10 km, the PGV distributions (Fig. 3) indicate different directions of rupture propagation for these two events. In addition, there are two high-PGV zones for the 0918 event in Fig. 3. One is close to the epicenter near the station F004, and the other is along the LVF between 23.3°N and 23.5°N. Figures 2 and 3 also present the locations of 15 damaged/collapsed buildings and bridges (marked by diamonds) from Chou et al. (2022). Because the time interval between both events is small, we cannot separate the damaged structures caused by each earthquake. However, on the basis of the ground motion distributions, three damaged buildings or bridges (No. 8 Wanan Elementary School, No. 14 Dianguang Bridge, and No. 15 Baohua Bridge) may have been damaged by the 0917 event (Figs. 2a and 3a); the remaining damage is considered to have been caused by the 0918 event.

2 Methods and results

To understand the source properties for the 0917 and 0918 events, we adopted the EGF method to investigate the rupture behaviors in the SMGA, such as the size, rupture velocity, rupture direction, stress drop, and contribution to strong ground motions. Then, we introduced the SSA method to estimate the centroid location of

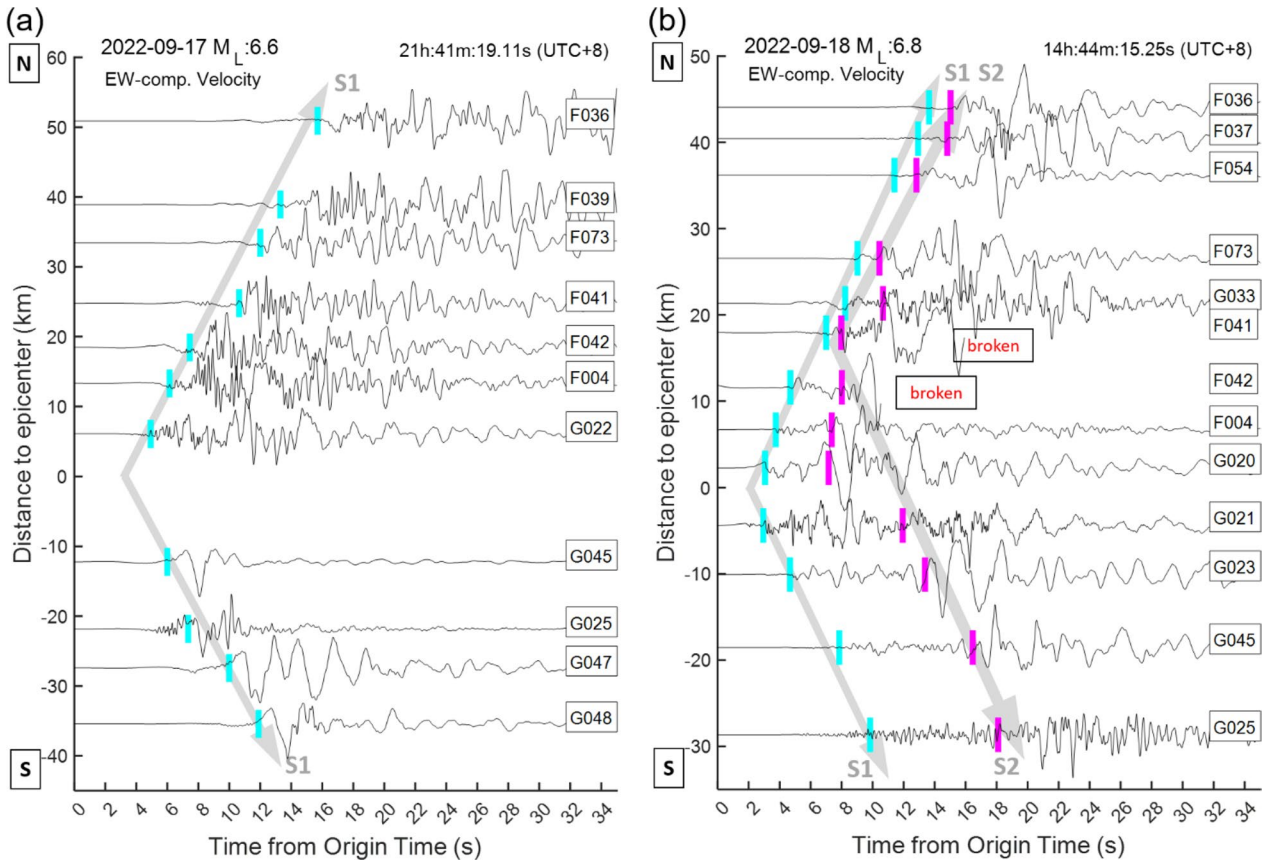

Fig. 4 N–S recorded section of the E–W component of velocity waveforms according to the distance to the epicenter. (**a**) For the 0917 event, data from 11 stations were used. The observed S-wave arrival times for the SMGA are marked in cyan–blue. (**b**) For the 0918 event, data from 13 stations were used. The observed S-wave arrival times for SMGA1 are marked in cyan–blue, and those for SMGA2 are marked in magenta

potential slip patches, which is the point at which large amplitudes of S-waves are generated during the rupture. The details are described below.

2.1 EGF analysis

The velocity waveforms in Fig. 4 show that the 0917 event has a single SMGA due to one distinct wave packet in Fig. 4a, whereas the 0918 event displays two clear wave packets in Fig. 4b, suggesting the presence of two SMGAs. For the 0917 event, we identified the S-wave arrival time (S1, Fig. 4a) of the SMGA at 11 stations located along the source region. Similarly, for the 0918 event, we determined the arrival times of SMGA1 (S1) and SMGA2 (S2) at 13 stations (Fig. 4b). We determined the S-wave arrival times primarily through visual inspection. To aid in the identification process, we applied various filtering bands to enhance the clarity of the waveforms, which helps to recognize the wave packets more accurately. Both acceleration and velocity waveforms of the EW and NS components were used to improve reliability. This procedure allowed us to iteratively refine the arrival times on the basis of station-specific characteristics and event variations. Before conducting EGF analysis, we objectively determined the rupture starting point and rupture time for each SMGA by employing a grid search method, as proposed by Asano and Iwata (2012), to obtain the optimal rupture initiation location.

To obtain the starting point of the SMGA, we used a small-magnitude earthquake very close to the target events as a reference (called the REF event), as listed in Table 1. The REF event was only used to identify the S-wave arrival time at each station, and its focal mechanism was not restricted. We applied a 3D velocity model (Huang et al. 2014) to calculate the travel times from the REF event as well as from the potential starting points of the SMGA at the stations and then estimated the RMS, which is defined as follows:

$$\mathrm{RMS} = \sqrt{\frac{1}{n}\sum_{i=1}^{n}\left[t_0 + (t^i_{cal} - \widehat{t}^i_{cal}) - (t^i_{obs} - \widehat{t}^i_{obs})\right]^2} \tag{1}$$

where t^i_{cal} and t^i_{obs} are the calculated and observed travel times of the starting point of the SMGA at the ith station, respectively. $\widehat{t}^i_{cal}$ and $\widehat{t}^i_{obs}$ are the calculated and observed travel times of the REF event. t_0 is the time delay of the starting point of the SMGA relative to the origin time of the target event. n is the number of stations used. In this study, we conducted a grid search across the fault plane with a spatial interval of 500 m in both the length and width directions and a temporal interval of 0.01 s. For the 0917 event, the fault plane was set to 55.4 km in length and 30.7 km in width, resulting in a total of 6,882 grid points. For the 0918 event, the fault plane was set to 77.6 km in length and 35.7 km in width, yielding 11,232 grid points. The grid search spanned the entire fault plane to ensure that all potential rupture starting points were included. The resulting distributions of the RMS residuals for the 0917 and 0918 events are shown in Fig. 5. The rupture starting points and delay times for each SMGA were determined by locating the grid point with the minimum RMS value, as summarized in Table 2.

In EGF analyses, for each investigated event (target event), we selected a small event that had a focal mechanism and hypocenter location similar to those of the respective target event as the EGF event (Fig. 6; Table 1), and 9 TSMIP stations were selected on the basis of the azimuthal coverage and the quality of seismograms for both the target event and the EGF events (Fig. 6). Adopting the rupture starting points as well as the rupture delay times in Table 2, the horizontal components of the acceleration, velocity, and displacement records in the frequency range of 0.2 to 10 Hz at four stations around the source region (solid triangles in Fig. 6) were simulated to estimate the optimal SMGA-related parameters, including the width (W) and length (L) of the SMGA, rupture velocity (Vr), and rise time (T), by applying source spectral ratio analysis and an EGF simulation (Irikura 1986; Miyake 1999; Miyake et al. 2003). More details of the EGF procedure are described in Appendix A and Lin et al. (2022). Here, we first performed EGF analyses for the 0917 event via a single-SMGA model. Figure 7a shows a comparison of the observed and synthetic waveforms at the stations used for the simulation (solid triangles in Fig. 6a). Figure 7b displays the waveform comparisons of other stations near the hypocenter (open triangles in Fig. 6a) for validation. Figure 14 displays a comparison of the observed and synthetic acceleration spectra. Most features of the observed records in the broadband frequency range could be well reproduced, suggesting that the simulation results were sufficiently reliable.

For the 0918 event, the two-SMGA model was applied. The first few seconds of observations were used to obtain the parameters of SMGA1, as listed in Table 3. Because the same EGF event was used for two SMGAs, we can rewrite Eq. (5) in Appendix A as

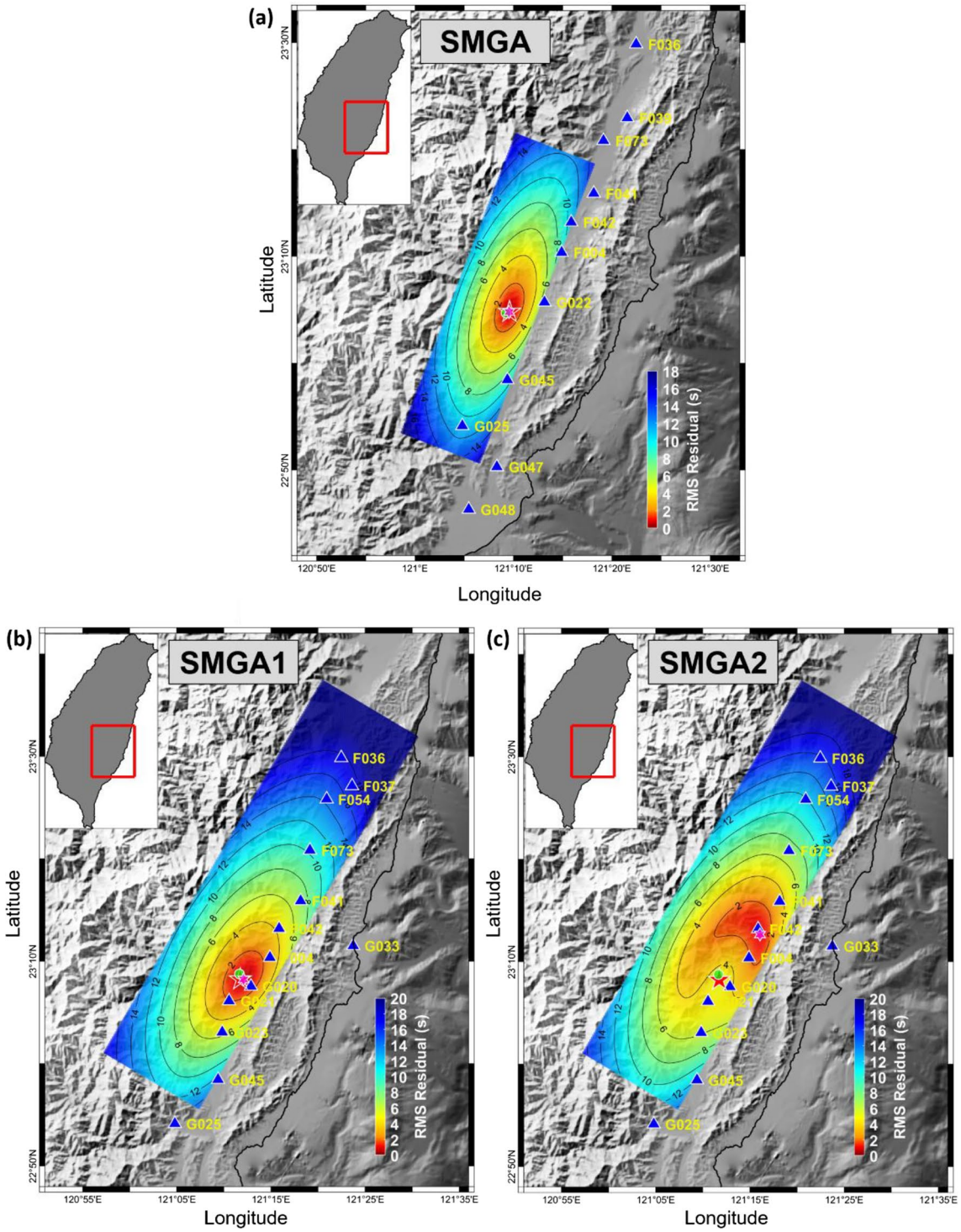

Fig. 5 Distributions of the RMS residuals derived via the grid search method for locating the rupture starting point (magenta pentagram) of (**a**) the SMGA of the 0917 event and (**b**) SMGA1 and (**c**) SMGA2 of the 0918 event. The red star marks the epicenter of the mainshock, and the solid green circle marks the reference event, both of which are determined via CWA data

Table 2 Locations of the rupture starting point and rupture delay time of the SMGA models for the 0917 and 0918 events.

		Longitude (°E)	Latitude (°N)	Depth (km)	Rupture time (s)
0917 Event	SMGA	121.1571	23.0805	9.05	0.26
0918 Event	SMGA1	121.2017	23.1369	7.57	0.26
	SMGA2	121.2678	23.2109	5.08	4.75

$$\frac{M_{0\_sum}}{m_0} = C_{sum}K_{sum}^3 = \frac{M_{0\_1} + M_{0\_2}}{m_0} = C_1K_1^3 + C_2K_2^3. \quad (2)$$

We assumed that the parameters obtained from the single-SMGA model represented the combined response of two SMGAs. Therefore, after obtaining C_1 and K_1 of SMGA1, we then derived C_2 and K_2. Applying the optimal parameters of SMGA1 with the location and delay time of Table 2, the related parameters of SMGA2 were then determined through the grid search, as listed in Table 3. The inaccuracy of the focal mechanism and attenuation effect might introduce errors into the synthetic waveforms. Figure 8 compares the observed records and the synthetic waveforms for the 2-SMGA model of the 0918 event, and Fig. 15 displays the comparison of the observed and synthetic acceleration spectra. The results indicate that the main characteristics of the observed waveforms for most stations could be sufficiently reproduced in the broadband range, except those at station F004. We discuss this in the discussion section.

2.2 SSA analysis

We considered both TSMIP and P-alert records for the SSA analysis. We converted a 50-s-long window of accelerations, starting from the origin time, to displacements via double integration, applied a zero-phase high-pass filter with a corner of 0.1 Hz, and then calculated their probability density functions (*PDF*s). The details of the SSA procedure are described in Lin et al. (2018). We considered the interrupted records, because these records were located at the key points

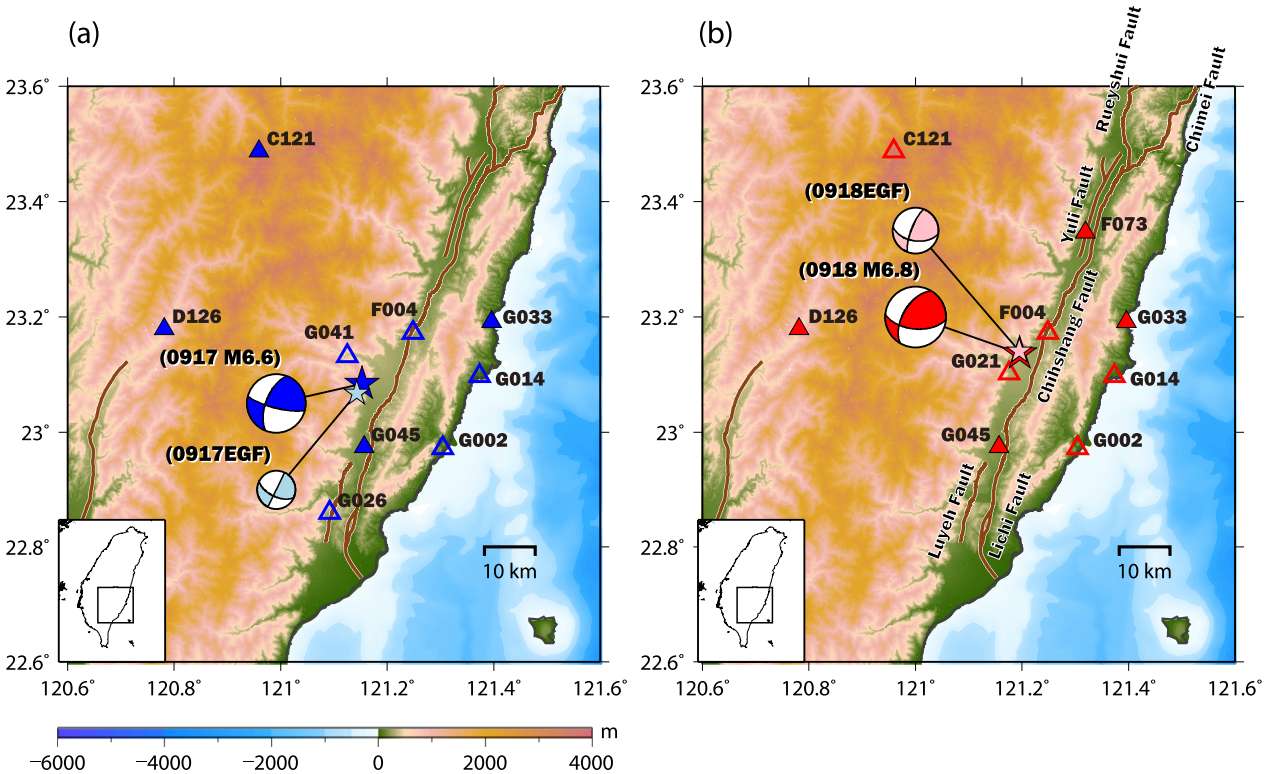

Fig. 6 Epicenters (stars) and focal mechanisms of the (**a**) 2022 Guanshan (0917) and (**b**) 2022 Chihshang (0918) earthquakes, as well as their EGF events. The triangles indicate the free-field strong-motion stations selected for the two events. The solid triangles represent the stations used in the source spectral ratio analysis and the EGF simulation. The open triangles represent the stations used in the forward ground motion simulation. The thick line is the active fault line of the CGS 2021 version

Table 3 Parameters of the SMGA models for the 0917 and 0918 events determined via strong-motion simulations.

		M_0 (10^{18}Nm)	K	C[a]	Rupture starting point[b]	L[c] (km)	W[d] (km)	V_r (km/s)	T[e] (s)	S[f] (km^2)	$\Delta\sigma_{SMGA}$[g] (MPa)
0917 event	SMGA	7.16	14	0.815	(5, 9)	5.6	8.4	2.96	0.98	384.38	18.9
0918 event	SMGA1	1.12	2	1.512	(2, 1)	5.6	3.6	2.52	0.2	111.96	12.8
	SMGA2	14.1	4	2.369	(4, 1)	10.0	6.0	2.55	1.0	604.12	23.3

[a] Stress drop ratio between target and EGF events; [b]rupture starting point defined as the initiation number of K (fault dimension ratio) along the strike and dip; [c]length of the strong motion generation area (SMGA); [d]width of the SMGA; [e]rise time for the mainshock; [f]rupture area estimated from the recipe of Irikura and Miyake (2011); and [g]stress drop of the SMGA

close to the faults/sources. The window of missing data was artificially filled with zeros. After obtaining the *PDF* for each station n, we determined the probability P at a source point (η) at a centroid delay (δ) as

$$\mathrm{P}(\eta,\delta)=\prod_{n=1}^{N}\sum_{m=-M}^{M}\left|PDF_N\left(\delta+t_{\eta\delta}+mdt\right)\right| \quad (3)$$

where N is the total *PDF*, and $t_{\eta\delta}$ is the propagation time of the S-wave from source η to a station n. We calculate the S-wave arrival time via the Taiwan 3D velocity structure proposed in Huang et al. (2014). dt is the time interval of 0.01 s, and M is the number of data points in half of the window around the arrival time (100 points). The source with the maximum probability was determined to be the centroid location (SSA location hereafter) for the event generating the largest amplitude of S-waves. Because our target was the generation area of the S-wave, we used both horizontal waveforms from stations located within a 50 km radius of the CWA epicenter. We applied the grid search approach to the study area, spanning from 120.9°E to 121.5°E in longitude and 22.85°N to 23.45°N in latitude. The horizontal grid interval in both directions was 0.025°. The vertical grid search range was from 0.0 to 30.0 km, with a 2.5 km interval. The centroid delay ranged from 0.0 to 20.0 s, with a 0.05 interval. The calculated parameters described above were both used in events 0917 and 0918, because their CWA epicenters were shallow and close.

Our results showed that the SSA location of the 0917 event was 7 km south of the CWA epicenter; the SSA location of the 0918 event was 14 km north of the CWA epicenter; the SSA depths were 2.5 to 5 km (Figs. 1 and 9); and the centroid delays for the 0917 and 0918 events were 5.25 and 9.40 s, respectively. Figure 10 displays the N–S record sections of the observed displacements normalized locally for both events, with the predicted P- and S-wave arrival times from the CWA hypocenter (bars T1 and T2) and from the SSA location (bars T3 and T4). For the 0918 event, we identified a clear S-phase moveout initiating at the SSA source along the T4 red bars (gray areas in Fig. 10b), and most arrival times of this phase matched the timings of the maximum amplitude at the stations (blue arrows in Fig. 10). We noticed that the stations near the CWA epicenter (i.e., F004, G061, G021, and G022) (Fig. 10b) exhibited maximum amplitudes earlier than the T4 bars do, consistent with the S-phase moveout initiating at the CWA hypocenter (T2 bars). These findings suggested that the displacements with large amplitudes at these stations were not related to the SSA source but rather to the CWA source. This corresponded with the two-SMGA model of the 0918 event from the EGF analysis. On the other hand, the observed displacements for the 0917 event at the stations located north of the CWA epicenter (e.g., F036, F039, F073, etc.) exhibited three obvious wave cycles (gray areas marked 1–3 in Fig. 10a) with similar amplitudes. These cycles caused a blunt distribution with lower probabilities in Fig. 9a than those for the 0918 event in Fig. 9b, causing greater uncertainty in the SSA location and centroid delay time for the 0917 event. In general, we have better confidence in the SSA location and centroid delay time for the 0918 event than in those for the 0917 event.

3 Discussion

3.1 Source properties of the 0917 and 0918 earthquakes

By analyzing the strong-motion records, we found that the rupture process of the 0918 event was more complex than that of the 0917 event (Fig. 11). Two SMGAs were determined on the CRF for the 0918 event. One occurred near the CWA epicenter and was 5.6 km in length and 3.6 km in width (dip direction), corresponding to an M 6.0 earthquake. Another was ~ 10 km north of the epicenter, with a larger area of 10.0 km in length and 6.0 km in width (dip direction), corresponding to an M 6.7 earthquake.

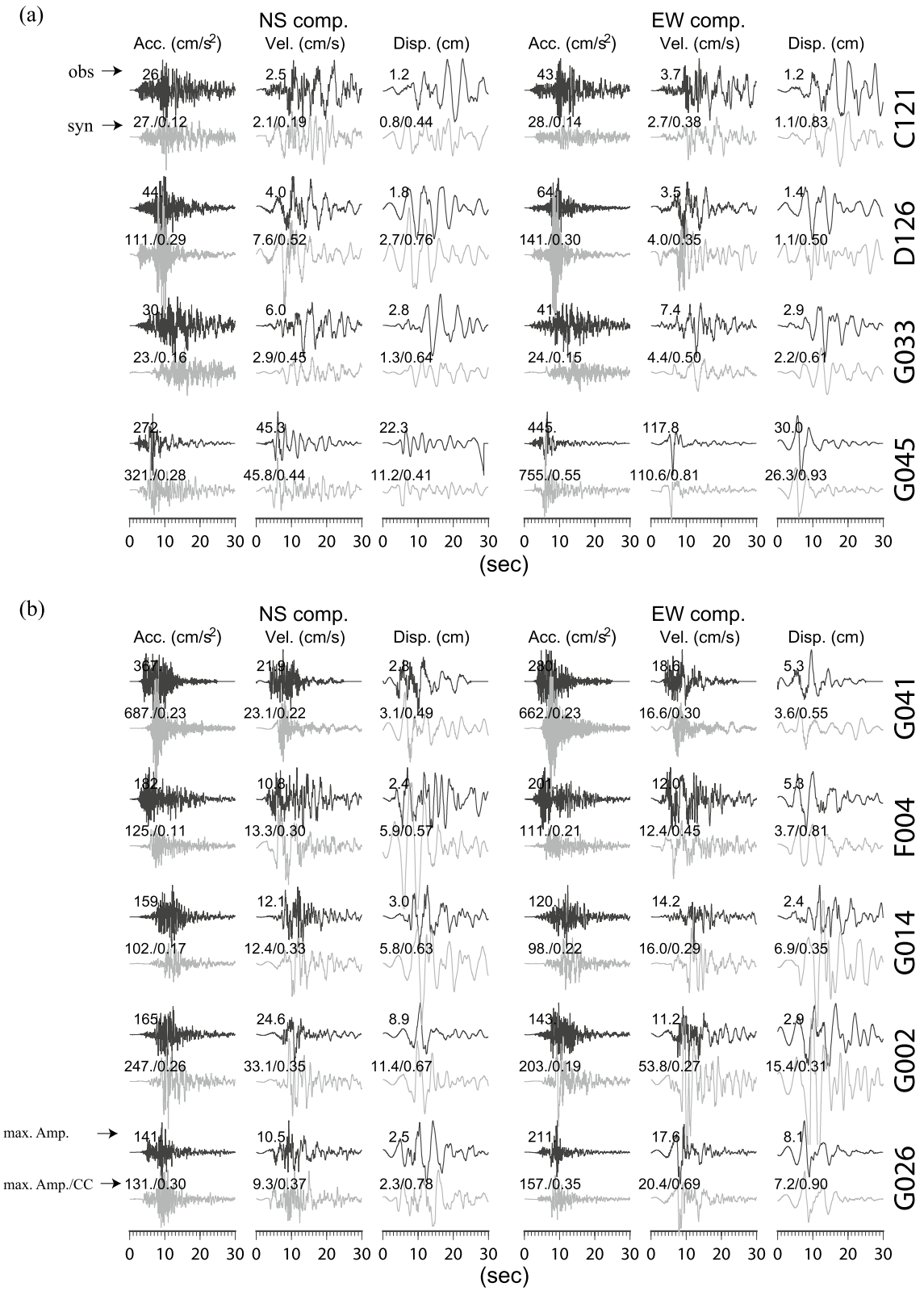

Fig. 7 Comparison of observed (black lines) waveforms from the 2022 Guanshan (0917) earthquake and synthetic (gray lines) waveforms at strong-motion stations (**a**) used for source modeling via the empirical Green's function method and (**b**) used for forward ground motion simulations. The maximum amplitudes and the cross-correlation coefficients (CCs) of the synthetic and observed data are shown above the traces. The starting point of the model is set at the CWA hypocenter

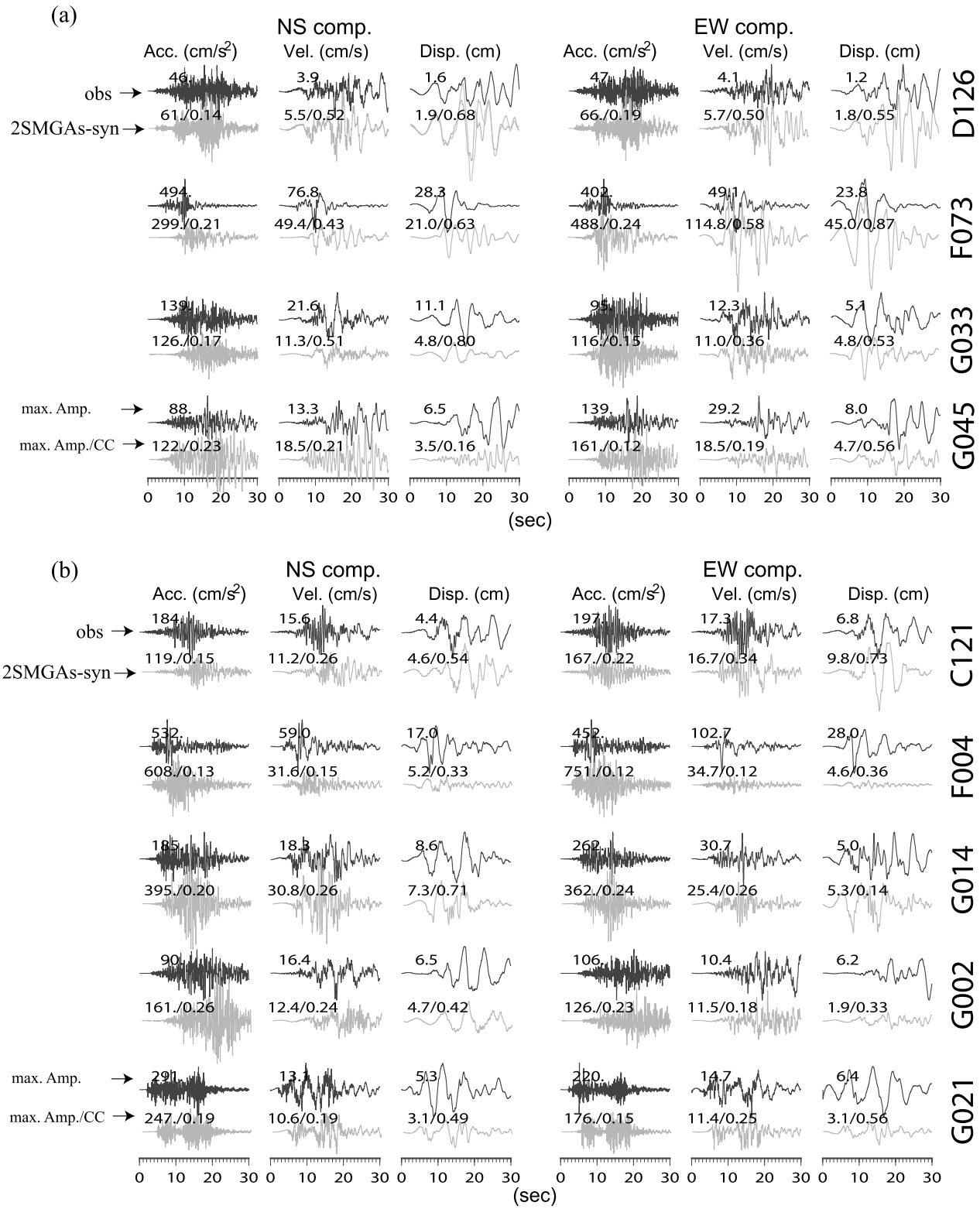

Fig. 8 Comparison of observed (black lines) waveforms from the 2022 Chihshang (0918) earthquake and synthetic (gray lines) waveforms at strong-motion stations (**a**) used for source modeling via the empirical Green's function method and (**b**) used for forward ground motion simulations. The maximum amplitudes and the cross-correlation coefficients (CCs) of the synthetic and observed data are shown above the traces. "obs" shows the observed record, and "2SMGAs-syn" shows the simulation from the two SMGAs model

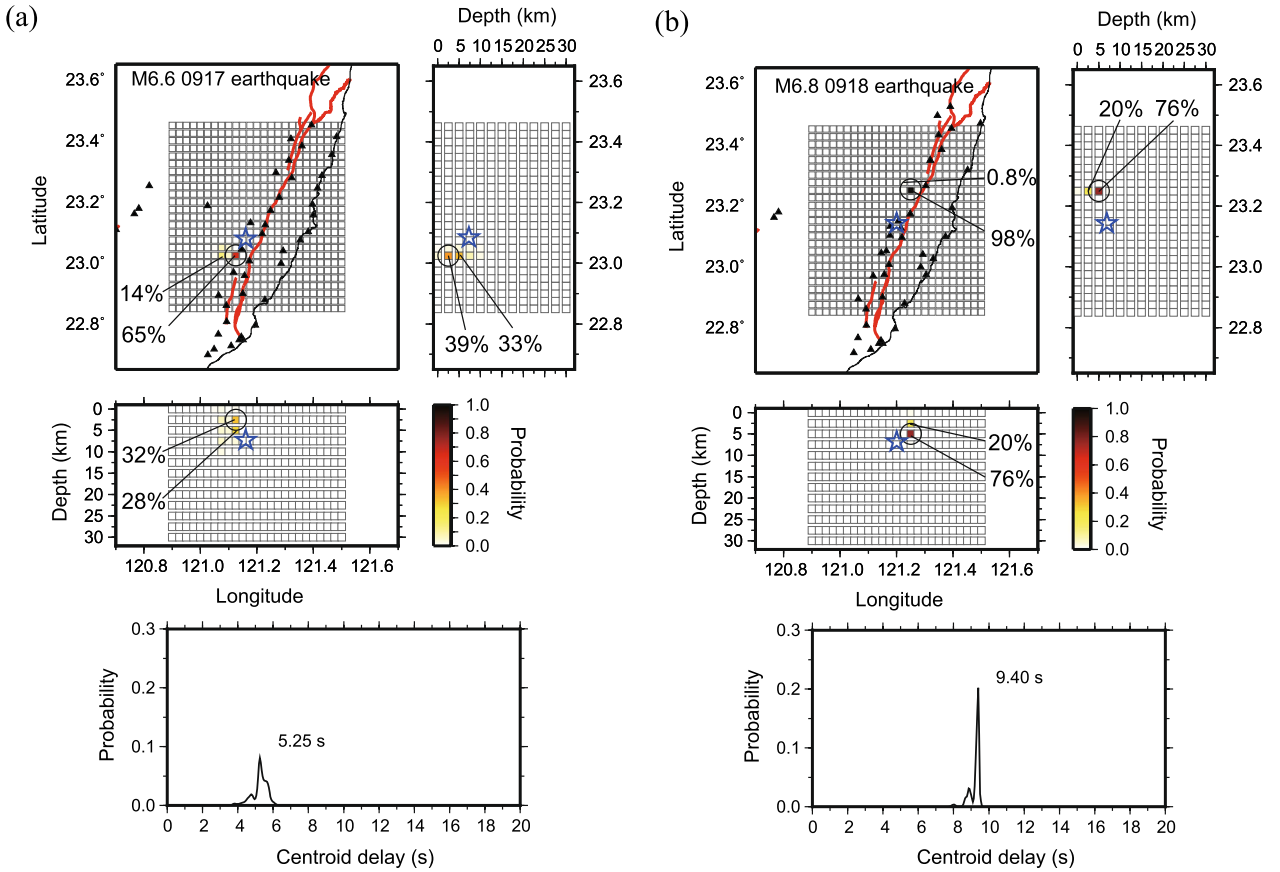

Fig. 9 SSA results for the (**a**) 0917 and (**b**) 0918 events. The map view, Z-E, and Z-N profiles of the probability distribution are shown. The open stars and circles are the CWA hypocenters and the SSA locations, respectively. The color scale shows the probability. The black triangles and red lines represent the stations selected for calculation and the active fault traces from the CGS 2021 version. The bottom sections demonstrate centroid delays of the events

The second SMGA was close to the 0918 SSA location. Both SMGAs of the 0918 event exhibited their own directivity to the north. Our two-SMGA source model explained the observations of the two high-PGV areas in Fig. 3, and the second SMGA was responsible for the collapsed/damaged buildings 20 ~ 40 km north of the epicenter.

For the 0917 event, there was only one SMGA near the CWA epicenter, which was 5.6 km in length and 8 km in width (dip direction). The rupture directivity was toward the south. The single-SMGA model for the 0917 event explained the high PGA and PGV areas in Figs. 2 and 3. Here, we noticed that the location of the SMGA was separate from the SSA location of both events (Fig. 11). This could be because we estimated the SSA location via displacement records whose frequency was lower than that of the acceleration records analyzed via the EGF method. This resulted in the EGF method having higher spatial and temporal resolutions in determining source properties than the SSA method. In addition, as described in "SSA Analysis" section, we have lower confidence in the 0917 SSA location because of the uncertainty produced by the three obvious cycles in Fig. 10. The 0917 SSA location should be closer to the epicenter, because the predicted arrival times (red bars) were always late than the arrival times for the maximum amplitude (blue arrows) at the stations in the southern region (i.e., G025, G047, and G048), as revealed in Fig. 10.

In general, our results are similar to those of the finite-fault slip model proposed in Lee et al. (2023) (Fig. 11). In detail, however, the size and location of the

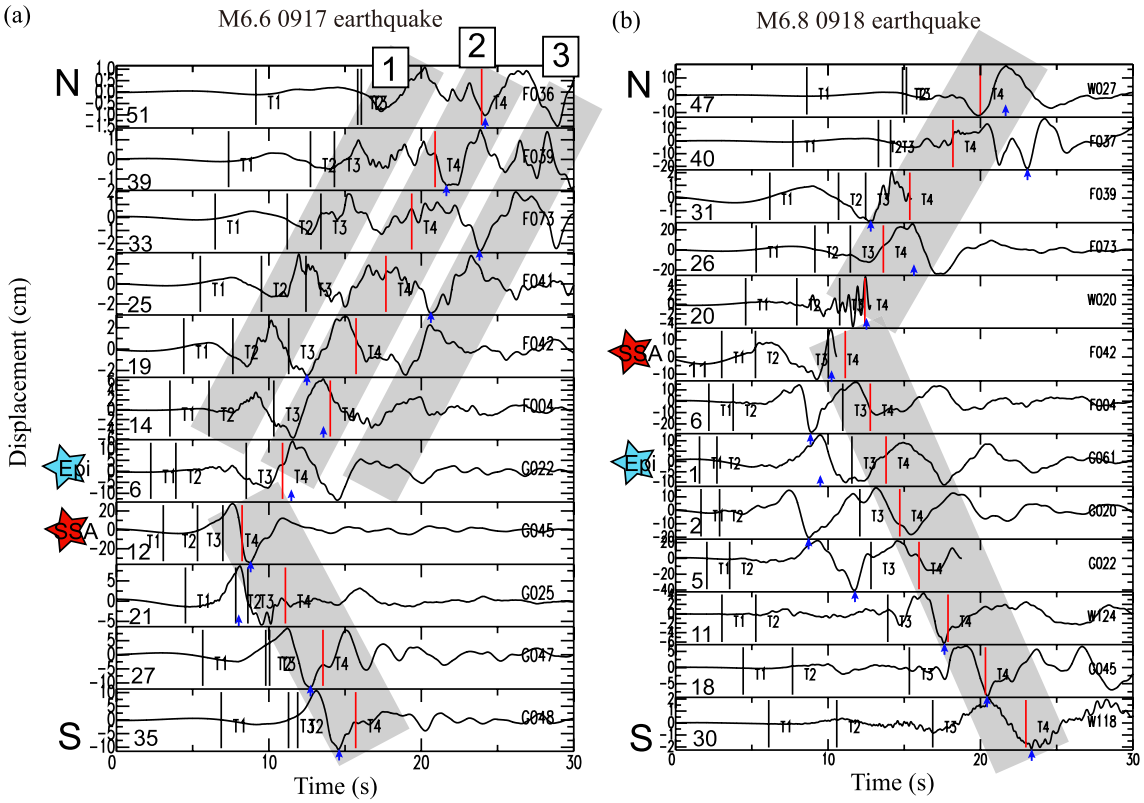

Fig. 10 N–S recorded section normalized locally for the E–W component displacements along the LV of the (**a**) 0917 and (**b**) 0918 events. The epicenter distance is shown on each trace. Predicted P- and S-wave arrival times from the CWA hypocenter (bars T1 and T2) and SSA location (bars T3 and T4) on the N–S recorded section. The blue and red stars represent the CWA epicenters and SSA locations, respectively. The blue arrows represent the maximum amplitudes at all the stations. The gray areas reveal the S-wave phase propagating from the SSA locations

SMGA models in the present study (using broadband data of 0.2 ~ 10 Hz) are slightly different from those of the slip model obtained via the finite-fault inversion method (using low-frequency data of 0.05 ~ 0.5 Hz). This result implies the multifrequency rupture process of the 0917 and 0918 events, while this property has been noted for some large earthquakes (M7 to M9) in the subducting areas, e.g., the 1994 M7.7 Sanriku–Oki earthquake (Nakayama and Takeo 1997), the 2007 M8.0 Pisco earthquake (Pulido et al. 2013), the 2010 M8.8 Chile earthquake (Kiser and Ishii 2011), and the 2011 Tohoku earthquake (Ide et al. 2011; Kurahashi and Irikura 2013; Wen 2014). Our result suggests that the multifrequency rupture process may also appear in moderate earthquakes (magnitude of 6 ~ 7) on a collision boundary.

3.2 Simulation of the high-amplitude velocity pulses

Most observed records in the broadband frequency range of both the 0917 and 0918 events could be well reproduced through the EGF analysis in both the time and frequency domains (Figs. 7, 8, 14, and 15), suggesting that the observed velocity pulses that damaged the buildings and structures were generated by the obtained SMGA(s) of both events. However, there was one exception, i.e., station F004, located between the two SMGAs of the 0918 event. Figures 8b and 15 show that the velocity and displacement amplitudes of the synthetics were much smaller than those of the observations, especially for the E–W component. The discrepancies in the amplitude and arrival time indicated that the velocity pulse at station F004 could not be explained by our model but still caused damage nearby (Fig. 3b), which requires further discussion.

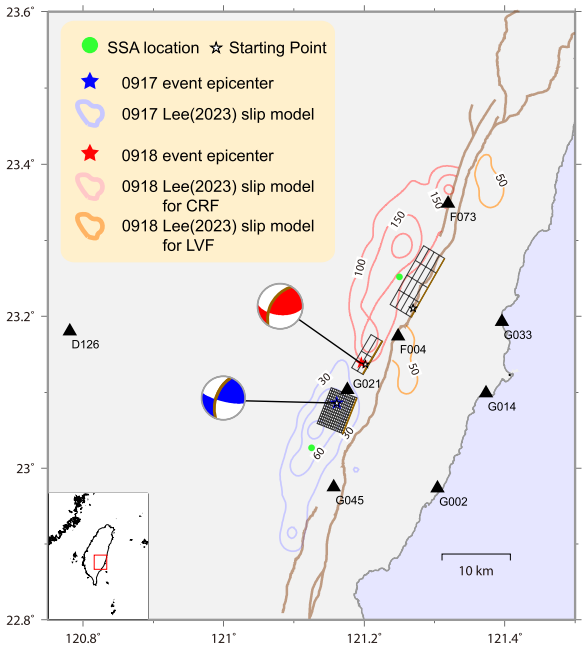

Fig. 11 Main slip areas of the slip models for the 0917 and 0918 events derived by Lee et al. (2023), with the CWA epicenters (stars) and SSA locations (circles). The black rectangles represent the SMGA models of both events, and the thick line represents the boundary close to the surface. The triangles indicate strong-motion stations. The thick lines are the active fault lines of the CGS 2021 version

We propose three possible causes for the large-amplitude record at station F004 for the 0918 event: (i) coseismic permanent deformation, (ii) instrumental problems, and (iii) local asperities close to station F004. We discuss the possibilities in order. First, coseismic permanent deformation resulting in a large velocity pulse (i.e., the fling effect) has been reported in previous studies (Huang et al. 2000; Bray and Rodriguez-Marek 2004; Burks and Baker 2014; Kamai et al. 2014; D'Amico et al. 2018). Station F004 is close to the surface line of the fault, and several surface ruptures and damage events have occurred in the nearby region (Figs. 2 and 3). However, the analyzed waveforms were filtered by a bandpass filter with two corner frequencies of 0.2 and 10 Hz. The permanent deformation should have already been removed. The waveforms were subjected to the permanent deformation correction procedure of Wu and Wu (2007), and we confirmed that the high amplitude was not related to permanent deformation (Fig. 16). Second, the instrument at station F004 may have malfunctioned due to artificial effects during the strong shaking of the 0918 event. Wen et al. (2001) reported that the extremely large PGA (~1 g) for the 1999 Chi–Chi earthquake recorded at station TCU129 was due to the effects of the concrete recording pier, not because of the source, path, and site effects. However, this possibility was eliminated, because the nearby P-alert station W01F (Fig. 1) also recorded high PGVs of 106 cm/s and 41 cm/s for the E–W and N–S components, respectively. In addition, station F004 was deployed exactly at the free field on the surface (Fig. 17), and no instrument issues were reported after the 0918 event. Finally, although both the 0917 and 0918 events mostly ruptured on the west-dipping CNF, the slip model and geological surveys showed that the east-dipping LVF also participated in the faulting process, especially for the 0918 event (CGS 2022; Lee et al. 2023). Figure 11 displays the slip model of Lee et al. (2023). In the shallow part of the east-dipping LVF, a thrust-slip patch (larger than 50 cm) occurred 6 ~ 10 s after initiation between the west-dipping SMGA1 and SMGA2 of the 0918 event. Because this slip patch was almost beneath station F004, it may have led to local strong motion and explain the earlier pulse as well as strong long-period energy, especially for the E–W component. This might also be because the synthetic waveform displayed insufficient energy between the wave packets of SMGA1 and SMGA2 for another close station, G021 (Fig. 8b). As more data and information are available, examining the role of the slip patch on the east-dipping LVF would be meaningful and interesting in future work.

3.3 Nonlinear site effect

Nonlinear site effects represent one potential factor influencing waveform amplitude estimation via the EGF method (Wen et al. 2020). Through the quantification of the nonlinear response, it becomes possible to reasonably explain one of the potential reasons for the overestimation of amplitudes in comparison with observations. In addition, the EGF method employs small-scale seismic events to simulate large-scale earthquakes and relies on a linear assumption. In general, small seismic amplitudes exhibit a linear site response, whereas larger seismic amplitudes, typically exceeding 100 cm/s^2, may induce nonlinear site effects. Nonlinear site effects are more prone to occur in soft-soil conditions. When nonlinear site effects manifest, they lead to a shift of predominant frequencies toward lower frequencies and the suppression of amplification factors, leading to lower-than-expected ground motion

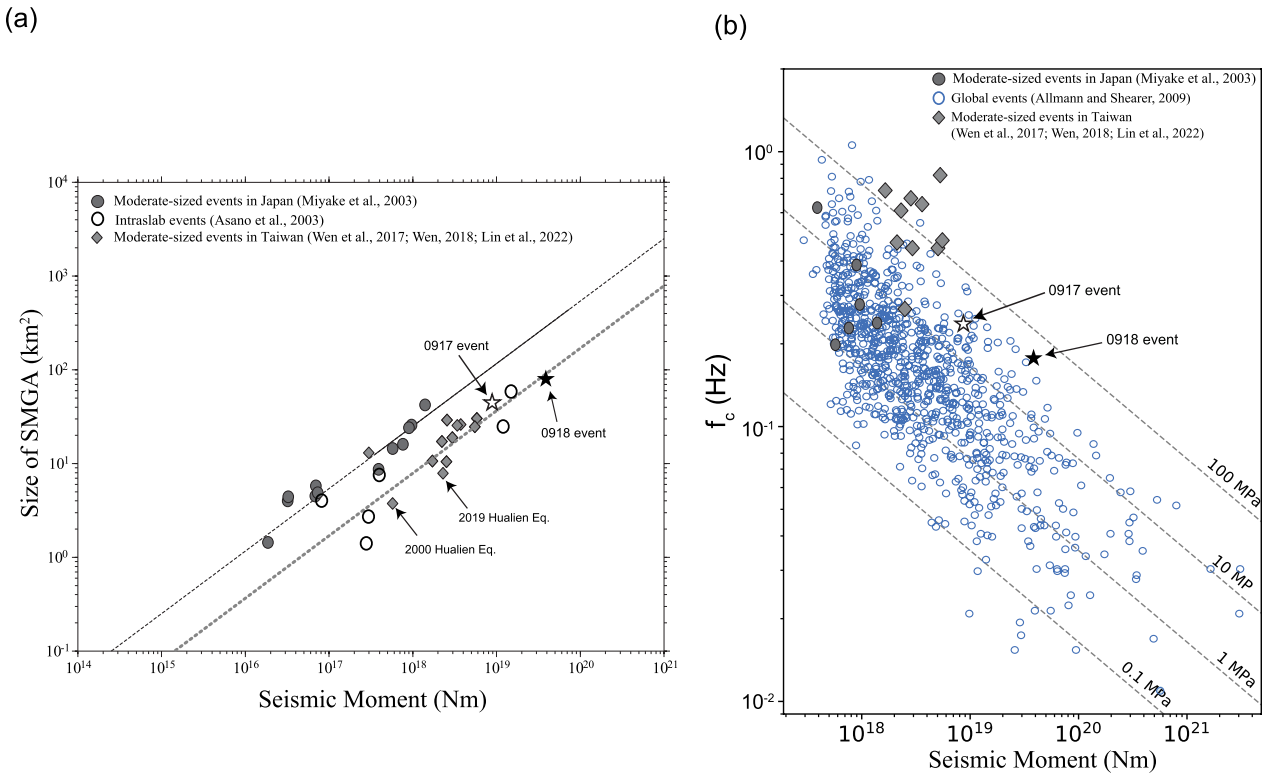

Fig. 12 (**a**) Scaling relation for the seismic moment versus the SMGA size. The solid line represents the empirical relationship between the combined area of asperities and the seismic moment for inland crustal earthquakes (Somerville et al. 1999), with the dashed lines as extensions for larger and smaller events. The dotted line indicates the empirical relation of Somerville et al. (1999) with a fivefold stress drop. The solid star shows our result of the combined dimension of the 2-SMGA model for the 0918 event. (**b**) Corner frequency as a function of the seismic moment. The dashed lines represent lines with a constant stress drop

amplitudes. This phenomenon has been substantiated in previous studies (Beresnev and Wen 1996; Boore et al. 1989; Noguchi and Sasatani 2008; 2011). To quantitatively assess nonlinear effects during strong seismic events, we followed the methodology outlined by Chen et al. (2017) to calculate the degree of nonlinearity (DNL), as shown in Fig. 18. For the 0917 event, seven stations were analyzed for nonlinear site responses. Stations C121, F004, G014, and G033 exhibited insignificant nonlinear site responses (DNL < 3.5), whereas G002 and G041 displayed minor nonlinear responses (DNL of approximately 4), and G045 demonstrated a more pronounced nonlinear response (DNL > 5). A significant site response during strong seismic observations may result in amplitude suppression due to the phenomenon of amplification suppression, leading to underestimation of the higher frequency portion when linear simulation techniques are used. A comparison of the observed and simulated amplitudes in the acceleration records (Fig. 7) revealed that for the four stations with insignificant nonlinear responses, the simulated amplitudes did not overestimate the observed values. However, G002, G041, and particularly G045, with the highest nonlinear response, showed instances of simulated amplitude overestimation. For the 0918 event, six stations were assessed for nonlinear response. Stations C121, G002, G014, and G033 displayed negligible nonlinear responses, whereas F004 and G045 exhibited stronger nonlinear responses (DNL > 6), which corresponded with the overestimation of the synthetic amplitude in the acceleration components, as shown in Fig. 8.

3.4 Stress drop of SMGAs in the 0917 and 0918 events

Previous studies have suggested that the high-angle west-dipping CNF in the southern LV serves as a boundary structure between the Central Range bedrock

and the remnants of the forearc basement from the lithosphere of the Philippine Sea Plate (Malavieille et al. 2002; Malavieille and Trullenque 2009; Shyu et al. 2011). The 2000 and 2019 Hualien earthquakes (Fig. 1), which ruptured in the deeper part of the northern CNF, revealed the properties of a small SMGA dimension and a high stress drop (Lin et al. 2022). What about the 0917 and 0918 events in the shallow part of the southern CNF? Fig. 12a shows the source scaling relationship between the size of the SMGA and the seismic moment. The SMGAs of moderate-sized earthquakes in Japan (solid circles in Fig. 12a) spatially coincided with almost the same area as the characterized asperity obtained via inversion models (Miyake et al. 2003). However, the SMGA dimensions of the 0917 and 0918 events (open and solid stars in Fig. 12a) followed the scaling relationship of buried earthquakes in Taiwan (including the 2000 and 2019 Hualien earthquakes) and shallow intraslab earthquakes in Japan, marked as diamonds and open circles in Fig. 12a, respectively (Asano et al. 2003; Wen et al. 2017; Wen 2018; Lin et al. 2022). This indicated relatively high stress drops on the SMGAs of the 0917 and 0918 events compared with inland crustal events. Using the scaling parameters C and K (see Appendix A), which are the ratios of the stress drops and fault dimensions between the target and EGF events, the seismic moment of each SMGA patch was calculated by multiplying the moment of the EGF event by CK^3 (Irikura 1986; Miyake et al. 2003). The seismic moments of the EGF events determined by the Broadband Array in Taiwan for Seismology (BATS) are listed in Table 1. We then followed the approach of Irikura and Miyake (2011) to estimate the stress drop in each SMGA and obtained values of 18.9 MPa for the SMGA of the 0917 event as well as 12.8 MPa for SMGA1 and 23.3 MPa for SMGA2 for the 0918 event (Table 3). Earthquake stress drop, which influences the level of high-frequency shaking that damages structures, is an important factor for seismic hazard analysis (Hanks and McGuire 1981; Boore 1983; Cotton et al. 2013). Previous studies have reported that stress drops vary with the tectonic environment and generally range between 0.1 and 100 MPa (open circles in Fig. 12b) (Kanamori and Anderson 1975; Allmann and Shearer 2009). Through the scaling relationship between the corner frequency (f_c) and the seismic moment, we found that the 0917 and 0918 events as well as the buried earthquakes in Taiwan (marked as stars and diamonds in Fig. 12b, respectively) indeed exhibited relatively greater stress drops than the events in Japan. Thus, locally high peak ground accelerations might be expected (Yen and Ma 2011). This may correspond to the intense ground shaking and severe damage caused by both events.

On the other hand, Cotton et al. (2013) demonstrated that the PGA is proportional to the stress drop and that an immature structure enhances the earthquake stress drop and strong ground motions (Manighetti et al. 2007; Radiguet et al. 2009). The low activity and absence of surface outcrops might suggest the immaturity of the CNF, which could explain the high stress drops and strong ground shaking during the 2013 Ruisui earthquake and the 2000 and 2019 Hualien earthquakes in the northern CNF (Wen et al. 2016; Lin et al. 2022) and the 0917 and 0918 events in the southern CNF. Although the 2019 Hualien earthquake also exhibited a two-SMGA pattern, its rupture was buried below a depth of 10 km and did not lead to the faulting of another structure. However, the 0918 event not only ruptured the shallow part of the CNF but also released energy on the LVF. This is similar to the 2018 Hualien earthquake, in which the rupture initiated at a shallow depth of 6 km on the CNF and propagated across the east-dipping Milun fault, and several surface ruptures caused damage (Wen et al. 2019). It is necessary to raise concern and carry out more studies of this not well-known but high-seismic-potential fault system.

4 Conclusions

Two disastrous events, the M_L 6.6 0917 and M_L 6.8 0918 events, which occurred on September 17 and 18, 2022, respectively, struck the southern LV of eastern Taiwan, causing unexpected damage. Our work documents seismic records from local strong-motion networks and damage situations for both events. Figure 1 shows the observed velocity waveforms with amplitudes > 60 cm/s. Figures 2 and 3 demonstrate the observed geometrical means of the PGA and PGV, as well as the seriously damaged structures for both events. To obtain the source properties of both events, we investigated the source properties for both events via higher and broader frequency-band waveforms (0.2 ~ 10 Hz) from local, dense strong-motion networks rather than those from finite-fault inversion (0.05 ~ 0.5 Hz) (Lee et al. 2023). EGF analyses revealed that the 0917 event ruptured to the south with a single SMGA, with a size of 47.04 km^2, and the 0918 event ruptured to the north through two SMGAs, with a combined size of 80.16 km^2. The stress drops for the SMGAs of events 0917 and 0918 were relatively high. The SSA analysis revealed that the centroid locations were located south and north of the CWA epicenters for the 0917 and 0918 events, respectively, and both locations were west of the surface line of the active fault in Taiwan, according to the CGS. This indicated

that the 0917 and 0918 events had southward directivity and northward directivity, respectively, and both occurred in the CNF. This finding was consistent with the results from the EGF analysis. In addition, the obtained SMGA models explained the observed records, except for the records at station F004 for the 0918 event. This may be because the 0918 event not only ruptured on the shallow part of the west-dipping CNF but also slipped on the east-dipping LVF, which caused a local strong-motion high-amplitude pulse to station F004 above the shallow slip patch. Combined with previous studies of moderate-to-large earthquakes occurring in the LV, we should pay attention to the interaction between the west-dipping CNF and the east-dipping LVF, especially for the shallow part above a depth of 10 km.

Appendix A

Following the ω^{-2} source spectral model of Brune (1970, 1971), the observed source spectral ratio of the target-to-EGF events was fitted by a theoretical function curve (Miyake 1999; Miyake et al. 2003):

$$\mathrm{SSRF}(f) = \frac{M_0}{m_0} \cdot \frac{1 + \left(\frac{f}{f_{ca}}\right)^2}{1 + \left(\frac{f}{f_{cm}}\right)^2}. \quad (4)$$

M_0 and m_0 are the seismic moments of the target-to-EGF events, respectively. f_{cm} and f_{ca} represent the corner frequencies of the target-to-EGF events. Applying the formulas of Irikura (1986) and Miyake et al. (2003), we obtained the scaling parameters C and K, which are the ratios of the stress drops and fault dimensions between the target event and the EGF event.

$$U_0/u_0 = M_0/m_0 = CK^3, K = f_{ca}/f_{cm} \quad (5)$$

where U_0/u_0 is the flat level of the displacement spectral ratio of the target-to-EGF events in the low-frequency range. Considering the probable rupture directivity effect, four strong-motion stations surrounding the source region (solid triangles in Fig. 6) were chosen for the source spectral ratio analysis in the broadband frequency range (0.2 to 10 Hz).

Using the 0917 event as an example, Fig. 13 shows the observed and fitted spectral ratios of the 0917 event to the EGF event. Through source spectral ratio fitting analysis, we obtained the scaling parameters $K=14$ and $C=0.815$. We then applied the EGF method to estimate the strong-motion generation area (SMGA), which was defined as $K \times K$ subfaults with dimensions equivalent to the rupture area of the EGF event (Irikura 1986; Irikura and Kamae 1994; Miyake et al. 2001). The optimal SMGA-related parameters, including the initiation position (rupture starting point), width (W) and length (L) of the SMGA, rupture velocity (Vr), and rise time (T), were then determined through a grid search in which the fitting residuals of the displacement records and acceleration envelopes were minimized (Miyake 1999):

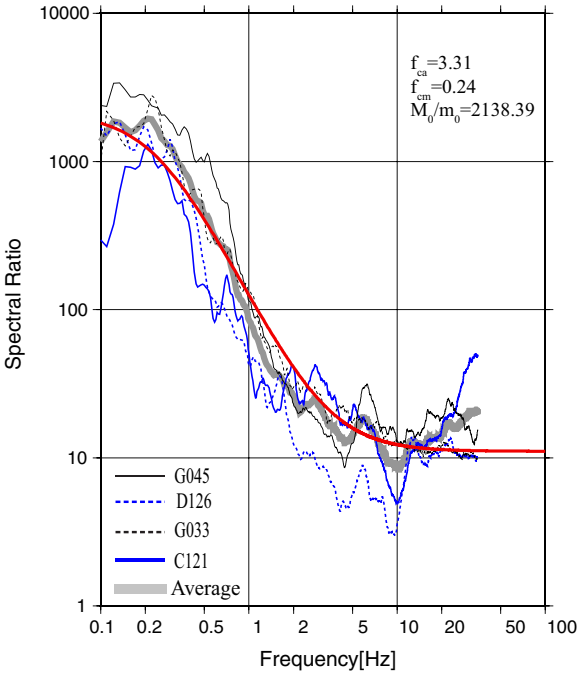

Fig. 13 Observed source spectral ratios of the stations used for source modeling, the average observed source spectral ratio (thick gray line), and the fitting source spectral ratio function (red line) for the 0917 event. The values of the parameters determined from the source spectral ratio fitting are listed

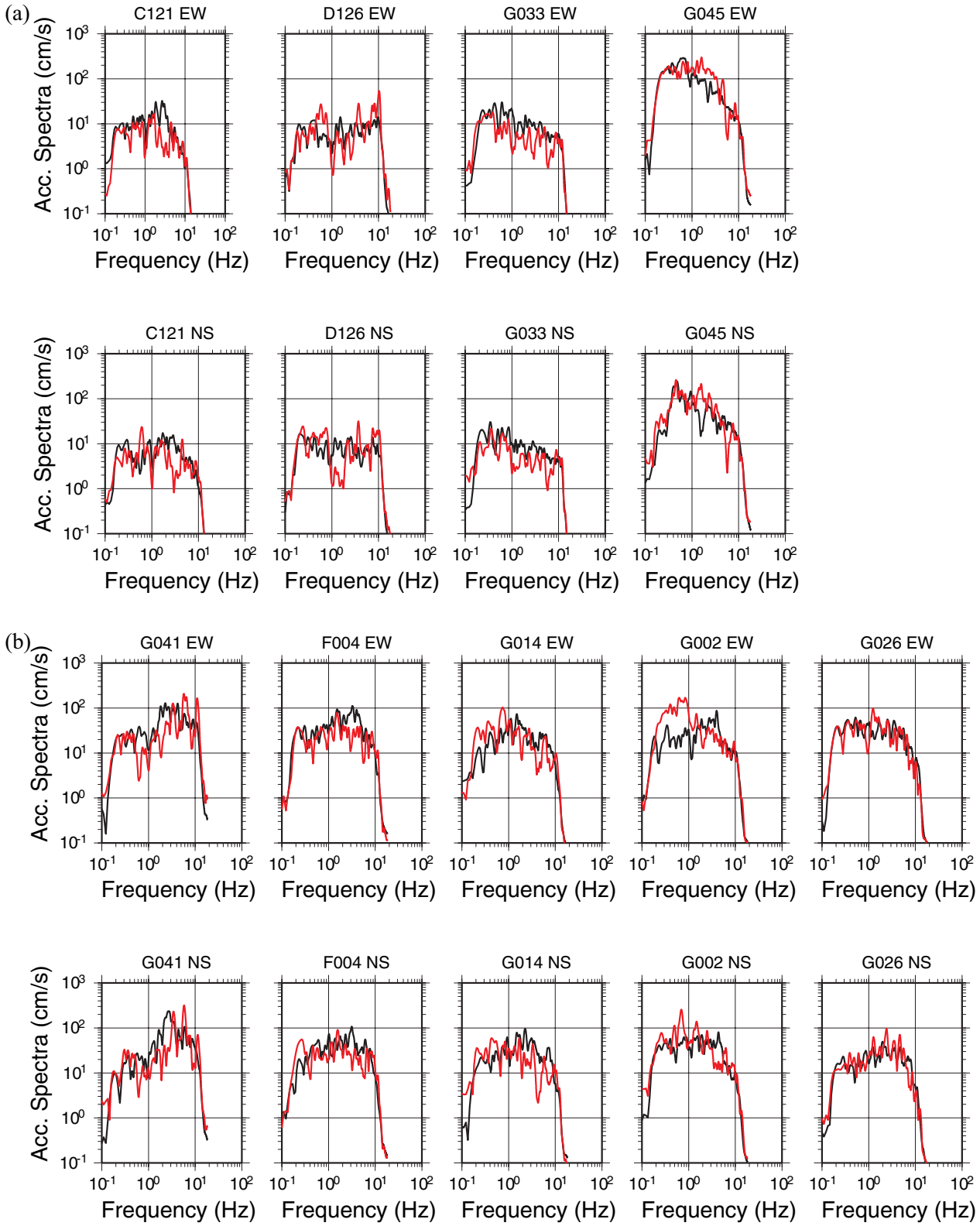

Fig. 14 Comparison of observed (black lines) and synthetic (red lines) acceleration spectra of the 0917 event at strong-motion stations (**a**) used for source modeling via the empirical Green's function method and (**b**) used for forward ground motion simulations. The frequency range used in this study is 0.2 to 10 Hz

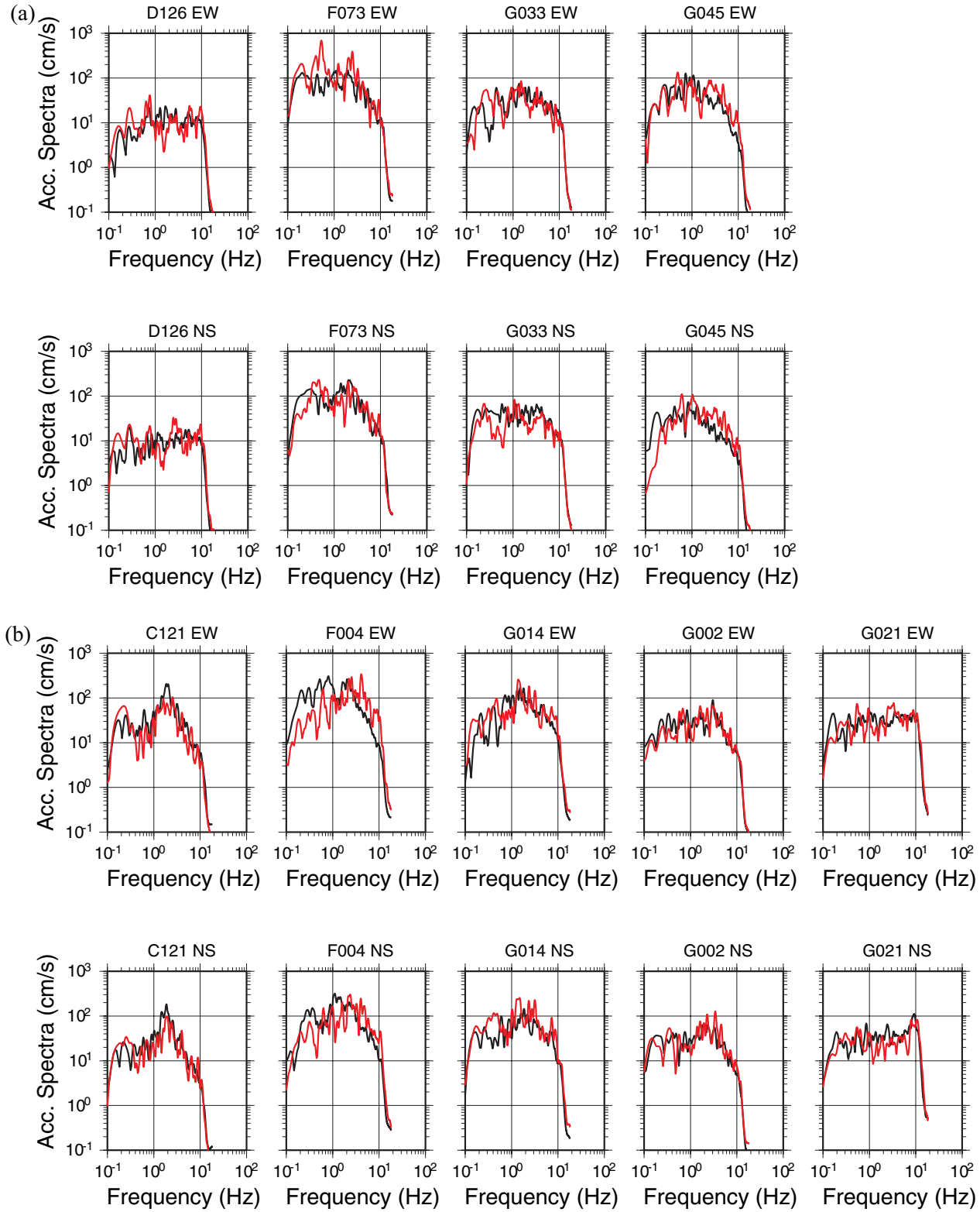

Fig. 15 Comparison of observed (black lines) and synthetic (red lines) acceleration spectra of the 0918 event at strong-motion stations (**a**) used for source modeling via the empirical Green's function method and (**b**) used for forward ground motion simulations. The frequency range used in this study is 0.2 to 10 Hz

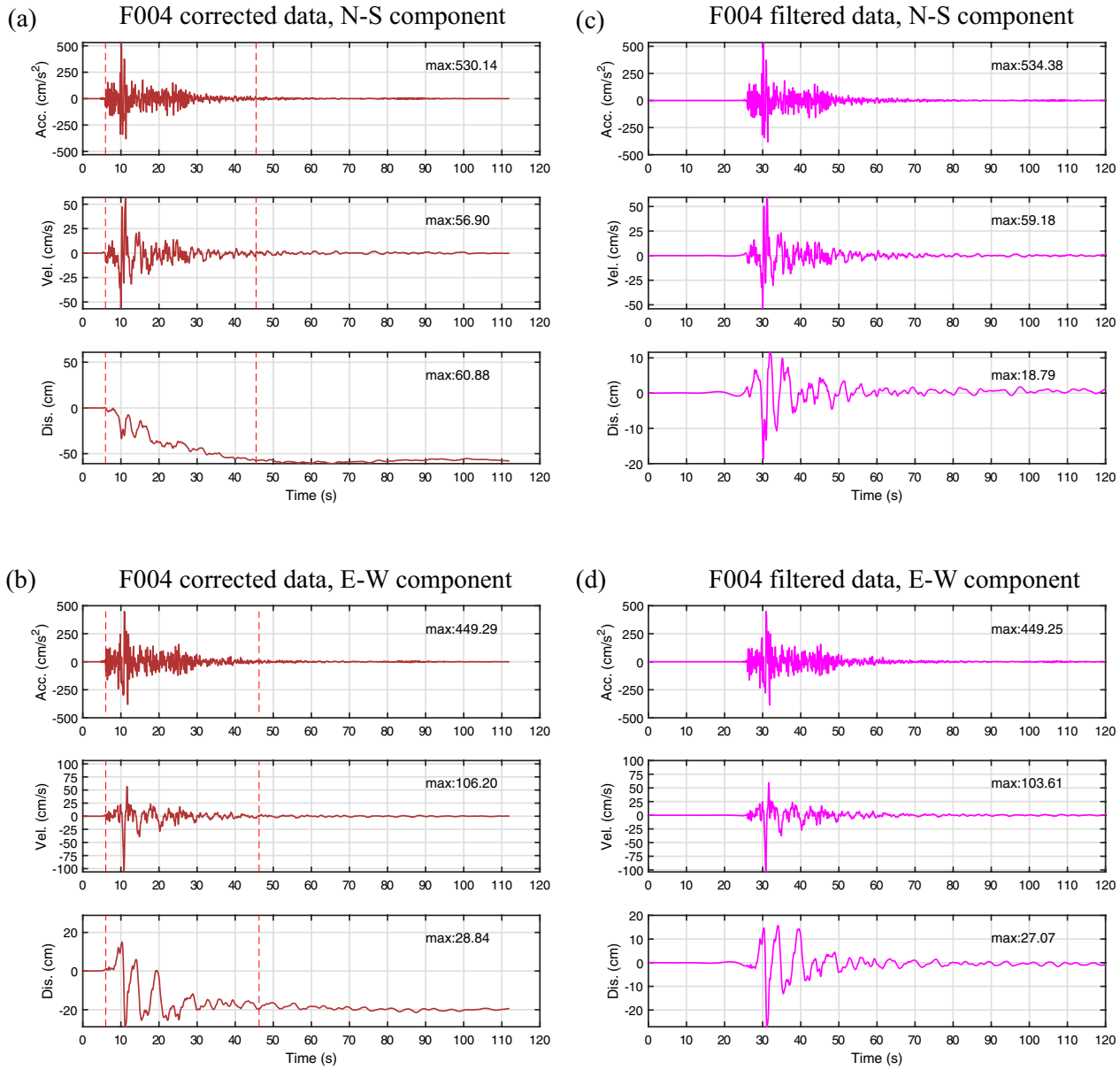

Fig. 16 Corrected seismic data of station F004 for the (**a**) N–S and (**b**) E–W components. Filtered seismic data of station F004 for the (**c**) N–S and (**d**) E–W components, with a frequency band of 0.1–10 Hz

Fig. 17 Station F004 was deployed exactly at the free field on the surface. The picture is from the GDMS database

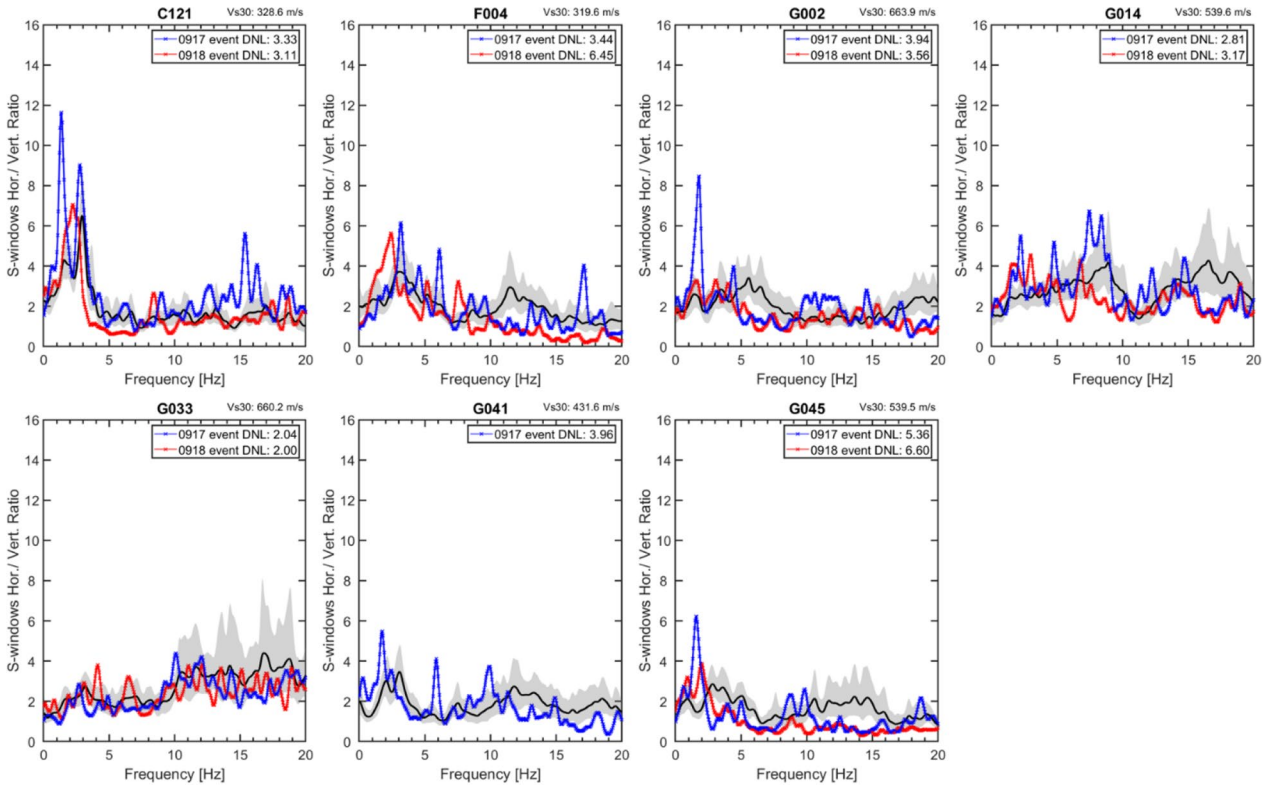

Fig. 18 Horizontal-to-vertical spectral ratio (HVSR) for the 0917 (blue line) and 0918 (red line) events. The black line represents the mean HVSR value of weak motions, with shadowed areas showing the one standard deviation range

Table 4 Search range and interval of the SMGA models for the 0917 and 0918 events.

		l, w (km)[a]	*Vr* (km/s)	τ (s)[b]
SMGA (0917 EGF)	Search range	0.2–4.0	1.7–3.2	0.01–0.3
	Interval	0.2	0.034	0.01
SMGA1 (0918 EGF)	Search range	0.2–3.0		
	Interval	0.2		
SMGA2 (0918 EGF)	Search range	0.5–4.0		
	Interval	0.5		

a: *l* and *w* are the length and width of the EGF, respectively; b: rise time of the EGF

$$\text{residual} = \frac{\sum_t (u_{obs} - u_{syn})^2}{\sqrt{(\sum_t {u_{obs}}^2)(\sum_t {u_{syn}}^2)}} + \frac{\sum_t \left(a_{env,obs} - a_{env,syn}\right)^2}{\left(\sum_t a_{env,obs}\right)\left(\sum_t a_{env,syn}\right)}. \quad (6)$$

where u_{obs} and u_{syn} are the observed and synthetic displacements, respectively. $a_{env,obs}$ and $a_{env,syn}$ represent the observed and synthetic acceleration envelopes, respectively. The search ranges and intervals of the model parameters are listed in Table 4.

See Figs. 13, 14, 15, 16, 17, 18.

Acknowledgements
We thank the Geophysical Database Management System (GDMS), developed by the Central Weather Administration (CWA) of Taiwan, and the Broadband Array in Taiwan for Seismology (BATS) for providing high-quality seismic data and focal mechanisms.

Author contributions
YYL performed the source-scanning algorithm analysis. YYW and YTY performed the broadband strong motion simulation, stress drop and scaling relationship analyses. YYL and YYW drafted the manuscript. CTC processed the strong-motion data and performed non-linear site effects analysis. YYW and YYL calibrated and improved the modeling results. YYL, YYW and YTY contributed to the discussion of the results. All authors participated in the discussion and the interpretation of the data. All authors read and approved the final manuscript.

Funding
This research has been supported by the National Science and Technology Council, Taiwan (Grant no. NSTC 112-2116-M-194-013, NSTC 112-2116-M-008-019, NSTC 113-2116-M-008-007 and NSTC 113-2116-M-194-012). The Taiwan Earthquake Center (TEC) contribution number for this article is 00194.

Availability of data and materials
Strong motion data was taken from the Geophysical Database Management System (GDMS), developed by Central Weather Administration (CWA) of Taiwan (https://gdmsn.cwa.gov.tw and Citation: https://doi.org/https://doi.org/10.7914/SN/T5), and is available by request. The fault plane solutions and seismic moment were determined by Global Centroid Moment Tensor (CMT) at https://www.globalcmt.org/CMTsearch.html and the Broadband Array in Taiwan for Seismology (BATS) at https://tecdc.earth.sinica.edu.tw/FM/AutoBATS/ (Citation: https://doi.org/https://doi.org/10.7914/SN/TW).

Declarations

Ethics approval and consent to participate
Not applicable.

Consent for publication
Not applicable.

Competing interests
The authors declare that they have no known competing financial interests or personal relationships that could have appeared to influence the work reported in this paper.

Author details
[1]Department of Earth Sciences, National Central University, Taoyuan 320317, Taiwan. [2]Earthquake-Disaster and Risk Evaluation and Management Center, National Central University, Taoyuan 320317, Taiwan. [3]The Graduate Institute of Applied Geology, National Central University, Taoyuan 320317, Taiwan. [4]Department of Earth and Environmental Sciences, National Chung Cheng University, Chia-Yi County 621301, Taiwan. [5]Southern Taiwan Earthquake Center, National Chung Cheng University, Chia-Yi County 621301, Taiwan. [6]Disaster Prevention Technology Research Center, Sinotech Engineering Consultants, Inc., Taipei 114065, Taiwan.

Received: 9 September 2024 Accepted: 13 December 2024
Published online: 11 March 2025

References

Allmann BP, Shearer PM (2009) Global variations of stress drop for moderate to large earthquakes. J Geophys Res. https://doi.org/10.1029/2008JB005821
Ammon CJ, Ji C, Thio H-K, Robinson D, Ni S, Hjorleifsdottir V, Kanamori H, Lay T, Das S, Helmberger D, Ichinose G, Polet J, Wald D (2005) Rupture process of the 2004 Sumatra-Andaman Earthquake. Science 308(5725):1133–1139. https://doi.org/10.1126/science.1112260
Asano K, Iwata T (2012) Source model for strong ground motion generation in the frequency range 0.1–10 Hz during the 2011 Tohoku earthquake. Earth Planet Space 64:1111–1123. https://doi.org/10.5047/eps.2012.05.003
Asano K, Iwata T, Irikura K (2003) Source characteristics of shallow intraslab earthquakes derived from strong-motion simulations. Earth Planet Space 55(4):e5–e8. https://doi.org/10.1186/BF03351744
Beresnev IA, Wen K-L (1996) Nonlinear site response—a reality? Bull Seismol Soc Am 86:1964–1978
Biq C (1965) The east Taiwan rift. Petroleum Geol Taiwan 4:93–106
Boore DM (1983) Stochastic simulation of high-frequency ground motions based on seismological models of the radiated spectra. Bull Seismol Soc Am 73(6A):1865–1894. https://doi.org/10.1785/bssa07306a1865
Boore DM, Seekins L, Joyner WB (1989) Peak accelerations from the 17 October 1989 Loma Prieta earthquake. Seismol Res Lett 60:151–166
Bray JD, Rodriguez-Marek A (2004) Characterization of forward-directivity ground motions in the near-fault region. Soil Dynam Earthq Eng 24(11):815–828. https://doi.org/10.1016/j.soildyn.2004.05.001
Burks LS, Baker JW (2014) Fling in near-fault ground motions and its effect on structural collapse capacity. In: Proceedings of the 10th National Conference in Earthquake Engineering, Earthquake Engineering Research Institute, Anchorage, AK
Central Geological Survey (2022) Geological survey report for 20220917 Guanshan and 0918 Chihshang earthquakes. Retrieved from https://reurl.cc/EoNygg (in Chinese)
Chen C-T, Chang S-C, Wen K-L (2017) Stochastic ground motion simulation of the 2016 Meinong, Taiwan Earthquake. Earth Planet Spaces 69:62. https://doi.org/10.1186/s40623-017-0645-z
Chou CC, Wu CL, Chai JF, Yao GC (2022) Reconnaissance report on seismic damage caused by Guanshan earthquake and Chihshang earthquake, Taiwan. National Center for Research on Earthquake Engineering, https://

www.ncree.narl.org.tw/assets/file/20220918_EQ_NCREE_V3.0.pdf. Accessed: 2 August 2023
Construction and Planning Agency (2011) Seismic design code and commentary for buildings. Construction and Planning Agency, Ministry of Interior Affair Chinese Taipei, Taiwan. (in Chinese)
Cotton F, Archuleta R, Causse M (2013) What is sigma of the stress drop? Seismol Res Lett 84(1):42–48. https://doi.org/10.1785/0220120087
D'Amico M, Felicetta C, Schiappapietra E, Pacor F, Gallovič F, Paolucci R, Puglia R, Lanzano G, Sgobba S, Luzi L (2018) Fling effects from near-source strong-motion records: insights from the 2016 Mw 6.5 Norcia, Central Italy, Earthquake. Seismol Res Lett 90(2A):659–671. https://doi.org/10.1785/0220180169
Hanks TC, McGuire RK (1981) The character of high-frequency strong ground motion. Bull Seismol Soc Am 71(6):2071–2095. https://doi.org/10.1785/bssa0710062071
Hickman JB, Wiltschko DV, Hung J-H, Fang P, Bock Y, Byrne TB, Liu C-S (2002) Structure and evolution of the active fold-and-thrust belt of southwestern Taiwan from Global Positioning System analysis. In: Geology and geophysics of an arc-continent collision, Taiwan. Geological Society of America 358:75–92. https://doi.org/10.1130/0-8137-2358-2.75
Huang B, Chen K, Huang W, Wang J, Chang D, Huang R, Chiu H, Tsai C (2000) Characteristics of strong ground motion across a thrust fault tip from the September 20, 1999, Chi-Chi, Taiwan earthquake. Geophys Res Lett 27:2729–2732
Huang H-H, Wu Y-M, Song X, Chang C-H, Lee S-J, Chang T-M, Hsieh H-H (2014) Joint Vp and Vs tomography of Taiwan: implications for subduction-collision orogeny. Earth Planet Sci Lett 392:177–191. https://doi.org/10.1016/j.epsl.2014.02.026
Ide S, Baltary A, Beroza GC (2011) Shallow dynamic overshoot and energetic deep rupture in the 2011 Mw 9.0 Tohoku-Oki Earthquake. Science 332:1425–1429. https://doi.org/10.1126/science.1207020
Irikura K (1986) Prediction of strong acceleration motions using empirical Green's function. In: Proceeding of 7th Japan Earthquake Engineering Symp, Tokyo, 10–12 December 1986, 151–156
Irikura K, Kamae K (1994) Estimation of strong ground motion in broad-frequency band based on a seismic source scaling model and an empirical Green's function technique. Ann Geophys 37:1721–1743
Irikura K, Miyake H (2011) Recipe for predicting strong ground motion from crustal earthquake scenarios. Pure Appl Geophys 168:85–104. https://doi.org/10.1007/s00024-010-0150-9
Jian PR, Tseng TL, Liang WT, Huang PH (2018) A new automatic full-waveform regional moment tensor inversion algorithm and its applications in the Taiwan area. Geophys Res Lett 108(2):573–587. https://doi.org/10.1785/0120170231
Kamai R, Abrahamson N, Graves R (2014) Adding fling effects to processed ground-motion time histories. Bull Seismol Soc Am 104(4):1914–1929. https://doi.org/10.1785/0120130272
Kan CW, Kao H, Ou GB, Chen RY, Chang CH (2010) Delineating the rupture planes of an earthquake doublet using Source-Scanning Algorithm: application to the 2005 March 3 Ilan Doublet, northeast Taiwan. Geophys J Int 182(2):956–966. https://doi.org/10.1111/j.1365-246X.2010.04664.x
Kanamori H, Anderson DL (1975) Theoretical basis of some empirical relations in seismology. Bull Seismol Soc Am 65(5):1073–1095. https://doi.org/10.1785/bssa0650051073
Kao H, Shan SJ (2004) The Source-Scanning Algorithm: mapping the distribution of seismic sources in time and space. Geophys J Int 157(2):589–594. https://doi.org/10.1111/j.1365-246X.2004.02276.x
Kao H, Shan SJ (2007) Rapid identification of earthquake rupture plane using Source-Scanning Algorithm. Geophys J Int 168(3):1011–1020. https://doi.org/10.1111/j.1365-246X.2006.03271.x
Kao H, Wang K, Chen RY, Wada I, He J, Malone SD (2008) Identifying the rupture plane of the 2001 Nisqually, Washington, earthquake. Bull Seismol Soc Am 98(3):1546–1558. https://doi.org/10.1785/0120070160
Kiser E, Ishii M (2011) The 2010 Mw 8.8 Chile earthquake: triggering on multiple segments and frequency-dependent rupture behavior. Geophys Res Lett 38:L07301. https://doi.org/10.1029/2011GL047140
Kurahashi S, Irikura K (2013) Short-period source model of the 2011 Mw 9.0 off the pacific coast of Tohoku Earthquake. Bull Seismol Soc Am 103(2B):1373–1393. https://doi.org/10.1785/0120120157
Lay T, Wallace TC (1995) Modern global seismology. Academic Press, Elsevier, San Diego
Lee JC, Angelier J, Chu HT, Hu JC, Jeng FS, Rau RJ (2003) Active fault creep variations at Chihshang, Taiwan, revealed by creep meter monitoring, 1998–2001. J Geophys Res 108(B11):2528. https://doi.org/10.1029/2003JB002394
Lee S-J, Liu T-Y, Lin T-C (2023) The role of the west-dipping collision boundary fault in the Taiwan 2022 Chihshang earthquake sequence. Sci Rep 13(1):3552. https://doi.org/10.1038/s41598-023-30361-0
Liao YC, Kao H, Rosenberger A, Hsu SK, Huang BS (2012) Delineating complex spatiotemporal distribution of earthquake aftershocks: an improved Source-Scanning Algorithm. Geophys J Int 189(3):1753–1770. https://doi.org/10.1111/j.1365-246X.2012.05457.x
Lin YY, Wen YY, Yen YT (2022) Source properties of the 2019 M_L6.3 Hualien, Taiwan, earthquake, determined by the local strong motion networks. Geophys J Int 229(3):1665–1679. https://doi.org/10.1093/gji/ggac003
Lin YY, Yeh TY, Ma KF, Song TRA, Lee SJ, Huang BS, Wu YM (2018) Source characteristics of the 2016 Meinong (M_L 6.6), Taiwan, earthquake, revealed from dense seismic arrays: double sources and pulse-like velocity ground motion. Bull Seismol Soc Am 108(1):188–199. https://doi.org/10.1785/0120170169
Liu KS, Shin TC, Tsai Y-B (1999) A free-field strong motion network in Taiwan: TSMIP. Terr Atmos Ocean Sci 10(2):377–396
Liu K-S, Tsai Y-B (2005) Attenuation relationships of peak ground acceleration and velocity for crustal earthquakes in Taiwan. Bull Seismol Soc Am 95(3):1045–1058. https://doi.org/10.1785/0120040162
Malavieille J, Lallemand SE, Dominguez S, Deschamps A, Lu C-Y, Liu C-S, Schnurle P, Crew A (2002) Arc-continent collision in Taiwan: New marine observations and tectonic evolution. Special Papers-Geological Society of America:187–211
Malavieille J, Trullenque G (2009) Consequences of continental subduction on forearc basin and accretionary wedge deformation in SE Taiwan: insights from analogue modeling. Tectonophysics 466(3):377–394. https://doi.org/10.1016/j.tecto.2007.11.016
Manighetti I, Campillo M, Bouley S, Cotton F (2007) Earthquake scaling, fault segmentation, and structural maturity. Earth Planet Sci Lett 253(3):429–438. https://doi.org/10.1016/j.epsl.2006.11.004
Miyake H, Iwata T, Irikura K (1999) Strong Ground motion simulation and source modeling of the Kagoshima-ken Hokuseibu Earthquakes of March 26 (M JMA 6.5) and May 13 (M JMA 6.3), 1997, Using Empirical Green's Function Method. Zisin. 51(4):431–442
Miyake H, Iwata T, Irikura K (2001) Estimation of rupture propagation direction and strong motion generation area from azimuth and distance dependence of source amplitude spectra. Geophys Res Lett 28(14):2727–2730. https://doi.org/10.1029/2000GL011669
Miyake H, Iwata T, Irikura K (2003) Source characterization for broadband ground-motion simulation: kinematic heterogeneous source model and strong motion generation area. Bull Seismol Soc Am 93(6):2531–2545. https://doi.org/10.1785/0120020183
Mozziconacci L, Delouis B, Huang BS, Lee JC, Béthoux N (2013) Determining fault geometry from the distribution of coseismic fault slip related to the 2006 Taitung Earthquake, Eastern Taiwan. Bull Seismol Soc Am 103(1):394–411. https://doi.org/10.1785/0120110232
Nakayama W, Takeo M (1997) Slip history of the 1994 Sanriku-Haruka-Oki, Japan, earthquake deduced from strong-motion data. Bull Seismol Soc Am 87:918–931. https://doi.org/10.1785/BSSA0870040918
Noguchi S, Sasatani T (2008) Quantification of degree of nonlinear site response. In: The 14th world conference on earthquake engineering, Oct 12–17, Beijing
Noguchi S, Sasatani T (2011) Nonlinear soil response and its effects on strong ground motions during the 2003 Miyagi-Oki intraslab earthquake. Zisin 63(3):165–187
Pulido N, Tavera H, Aguilar Z, Nakai S, Yamazaki F (2013) Strong motion simulation of the M8. 0 August 15, 2007, Pisco earthquake; effect of a multi-frequency rupture process. J Disaster Res 8(2):235–242
Radiguet M, Cotton F, Manighetti I, Campillo M, Douglas J (2009) Dependency of near-field ground motions on the structural maturity of the ruptured faults. Bull Seismol Soc Am 99(4):2572–2581. https://doi.org/10.1785/0120080340
Shyu JBH, Sieh K, Chen YG, Chung LH (2006) Geomorphic analysis of the Central Range fault, the second major active structure of the Longitudinal Valley suture, eastern Taiwan. GSA Bull 118(11–12):1447–1462. https://doi.org/10.1130/B25905.1

Shyu JBH, Wu Y-M, Chang CH, Huang HH (2011) Tectonic erosion and the removal of forearc lithosphere during arc-continent collision: evidence from recent earthquake sequences and tomography results in eastern Taiwan. J Asian Earth Sci 42(3):415–422. https://doi.org/10.1016/j.jseaes.2011.05.015

Shyu JBH, Yin YH, Chen CH, Chuang YR, Liu SC (2020) Updates to the on-land seismogenic structure source database by the Taiwan Earthquake Model (TEM) project for seismic hazard analysis of Taiwan. Terr Atmos Ocean Sci 31:469–478. https://doi.org/10.3319/TAO.2015.11.27.02

Somerville P, Irikura K, Graves R, Sawada S, Wald D, Abrahamson N, Iwasaki Y, Kagawa T, Smith N, Kowada A (1999) Characterizing crustal earthquake slip models for the prediction of strong ground motion. Seismol Res Lett 70(1):59–80. https://doi.org/10.1785/gssrl.70.1.59

Velasco AA, Ammon CJ, Lay T (1994) Empirical green function deconvolution of broadband surface waves: Rupture directivity of the 1992 Landers, California (Mw = 7.3), earthquake. Bull Seismol Soc Am 84(3):735–750. https://doi.org/10.1785/bssa0840030735

Wen KL, Peng HY, Tsai YB, Chen KC (2001) Why 1G was recorded at TCU129 site during the 1999 Chi-Chi, Taiwan, Earthquake. Bull Seismol Soc Am 91(5):1255–1266. https://doi.org/10.1785/0120000707

Wen YY (2014) Rupture behaviors of the 2011 Tohoku earthquake and its strongest foreshock through an empirical Green's function deconvolution analysis. J Asian Earth Sci 81:123–128. https://doi.org/10.1016/j.jseaes.2013.11.022

Wen YY (2018) Source characteristics of the northern Longitudinal Valley, Taiwan derived from broadband strong-motion simulation. Pure Appl Geophys 175:587–596

Wen YY, Chao SY, Yen YT, Wen S (2017) Source characteristics of moderate-to-strong earthquakes in the Nantou area, Taiwan: insight from strong ground motion simulations. Earth, Planet Space 69(1):132. https://doi.org/10.1186/s40623-017-0720-5

Wen YY, Wen S, Lee YH, Ching KE (2019) The kinematic source analysis for 2018 Mw 6.4 Hualien, Taiwan Earthquake. Terr Atmos Ocean Sci 30:377–387. https://doi.org/10.3319/TAO.2018.11.15.03

Wen YY, Yen YT, Kuo CH, Ching KE (2020) Source and strong-motion characteristics of two M > 6 buried earthquakes in southwest Taiwan. Earth, Planet Space 72(1):188. https://doi.org/10.1186/s40623-020-01322-y

Wen YY, Yen YT, Wen S, Lee SJ, Kuo CH, Lin YY (2016) Hybrid ground motion simulation for the 2013 M_L 6.4 Ruisui, Taiwan earthquake. Terr Atmos Ocean Sci 27(3):407–414. https://doi.org/10.3319/TAO.2015.10.30.01(TEM)

Wu YM, Chen DY, Lin TL, Hsieh CY, Chin TL, Chang WY, Li WS, Ker SH (2013) A high-density seismic network for earthquake early warning in taiwan based on low cost sensors. Seismol Res Lett 84(6):1048–1054. https://doi.org/10.1785/0220130085

Wu YM, Chen YG, Chang CH, Chung LH, Teng TL, Wu FT, Wu CF (2006) Seismogenic structure in a tectonic suture zone: with new constraints from 2006 Mw6.1 Taitung earthquake. Geophys Res Lett. https://doi.org/10.1029/2006GL027572

Wu YM, Liang WT, Mittal H, Chao WA, Lin CH, Huang BS, Lin CM (2016) Performance of a low-cost earthquake early warning system (P-Alert) during the 2016 ML 6.4 Meinong (Taiwan) Earthquake. Seismol Res Lett 87(5):1050–1059. https://doi.org/10.1785/0220160058

Wu YM, Wu CF (2007) Approximate recovery of coseismic deformation from Taiwan strong-motion records. J Seismol 11(2):159–170. https://doi.org/10.1007/s10950-006-9043-x

Yagi Y, Okuwaki R, Enescu B, Lu J (2023) Irregular rupture process of the 2022 Taitung, Taiwan, earthquake sequence. Sci Rep 13(1):1107. https://doi.org/10.1038/s41598-023-27384-y

Yen YT, Ma KF (2011) Source-scaling relationship for M 4.6–8.9 earthquakes, specifically for earthquakes in the collision zone of Taiwan. Bull Seismol Soc Am 101(2):464–481. https://doi.org/10.1785/0120100046

Yu SB, Chen HY, Kuo LC (1997) Velocity field of GPS stations in the Taiwan area. Tectonophysics 274(1):41–59. https://doi.org/10.1016/S0040-1951(96)00297-1

Yu SB, Kuo LC (2001) Present-day crustal motion along the Longitudinal Valley Fault, eastern Taiwan. Tectonophysics 333(1):199–217. https://doi.org/10.1016/S0040-1951(00)00275-4

Publisher's Note